AGU PUBLICATIONS

JGR

Journal of Geophysical Research: Space Physics

RESEARCH ARTICLE

10.1002/2016JA023594

Key Points:
- We quantify variability of observed ion flow shears, showing this is the major driver of variability of cusp satellite drag/density
- We also quantify variability in plasma density below 200 km, as the next most significant driver perturbing cusp satellite drag/density
- Our data show that correlation studies require sorting using this complementary essential physics, to explain variable drag

Correspondence to:
Å. S. Skjæveland,
asmund.skjaveland@fys.uio.no

Citation:
Skjæveland, Å. S., H. C. Carlson, and J. I. Moen (2017), A statistical survey of heat input parameters into the cusp thermosphere, *J. Geophys. Res. Space Physics*, *122*, doi:10.1002/2016JA023594.

Received 16 OCT 2016
Accepted 27 JUL 2017
Accepted article online 31 JUL 2017

A statistical survey of heat input parameters into the cusp thermosphere

Åsmund Steen Skjæveland[1,2], Herbert C. Carlson[3], and Jøran Idar Moen[1,2]

[1]Department of Physics, University of Oslo, Oslo, Norway, [2]University Centre in Svalbard, Longyearbyen, Norway, [3]Space Weather Center, CASS, Utah State University, Logan, Utah, USA

Abstract Based on three winters of observational data, we present those ionosphere parameters deemed most critical to realistic space weather ionosphere and thermosphere representation and prediction, in regions impacted by variability in the cusp. The CHAMP spacecraft revealed large variability in cusp thermosphere densities, measuring frequent satellite drag enhancements, up to doublings. The community recognizes a clear need for more realistic representation of plasma flows and electron densities near the cusp. Existing average value models produce order of magnitude errors in these parameters, resulting in large underestimations of predicted drag. We fill this knowledge gap with statistics-based specification of these key parameters over their range of observed values. The European Incoherent Scatter Svalbard Radar tracks plasma flow V_i, electron density N_e, and electron, ion temperatures T_e, T_i, with consecutive 2–3 min windshield wipe scans of 1000 × 500 km areas. This allows mapping the maximum T_i of a large area within or near the cusp with high temporal resolution. In magnetic field-aligned mode the radar can measure high-resolution profiles of these plasma parameters. By deriving statistics for N_e and T_i, we enable derivation of thermosphere heating deposition under background and frictional drag-dominated magnetic reconnection conditions. We separate our N_e and T_i profiles into quiescent and enhanced states, which are not closely correlated due to the spatial structure of the reconnection foot point. Use of our data-based parameter inputs can make *order of magnitude* corrections to *input* data driving thermosphere models, enabling removal of previous twofold drag errors.

Plain Language Summary Input of energy into the polar ionosphere from the solar wind causes local heating and upwelling of air in the region known as the "cusp." This upwelling in turn dramatically changes the density of the atmosphere as it rises, which has consequences for atmospheric composition and transport as well as for spacecraft that experience increased drag and possibly shortened lifetimes. We show that because of the highly dynamic nature of the cusp, long-term averages and models will not accurately reproduce the energy input to the cusp and the consequent upwelling of the air. We use empirical data to show that the energy input is highly dynamic and that it is necessary to separate active and quiet periods when modeling heating and upwelling in the cusp, as well as to detect or predict accurately where the cusp is located. We present statistical models of the active and quiescent cusp ionization density and temperature of the ionized gas. Occurrence rates of heating events in and near the cusp are estimated by using rapid radar scans covering a large area.

1. Introduction

Variability of the neutral density over the cusp and polar regions is now recognized as an important space weather phenomenon for satellite operators. *Lühr et al.* [2004] observed unexpected strong enhancements of satellite drag and upper thermosphere density over the cusp, repeatedly far outside the range of errors expected or needed from prediction or specification models. Based on *Carlson* [1998], it was shown that the nonlinear response of the thermosphere, to known ionospheric variability (specifically plasma flow speeds, and bottomside ionosphere electron density/conductivity), can [*Carlson*, 2007] and does [*Carlson et al.*, 2012] account for the drag prediction errors. The community has now reached full consensus that more realistic values for these two parameters is essential to improved forecast and specification [*Crowley et al.*, 2008, 2010; *Rentz and Lühr*, 2008; *Prölss*, 2010; *Carlson et al.*, 2012; *Sadler et al.*, 2012; *Wilder et al.*, 2012; *Zhang et al.*, 2012; *Deng et al.*, 2013].

However, plasma flow shears and electron densities below 200 km cannot be determined a priori; their values can only come from measured morphology. Because this specification requires altitude profiles of these parameters to be measured with time continuity over large areas in the vicinity of the cusp, such very limited data exist. The purpose of this study is to fill this information gap, to meet this pressing need.

Since 2004, morphological definition of cusp density and drag has been well documented by Lühr and colleagues. Near 400 km the cusp shows density/drag enhancements both more significant and persistent than any other location of the globe—in this regard it is unique. Over half of all satellite passes over the cusp near 400 km show density enhancements in excess of 20%, average enhancement of ~33% with no seasonal variation [*Kervalishvili and Lühr*, 2013], and enhancements up to doubling. Intense fine scale currents are associated with the density enhancements. *Kervalishvili and Lühr* [2013] and *Lühr et al.* [2004] both suggested upwelling of the cusp thermosphere as the only plausible explanation for these density bulges and suggested Joule heating as the cause of the heating leading to the upwelling. The density/drag enhancement over the cusp observed with the CHAMP spacecraft, documented by *Lühr et al.* [2004], has received much attention over the past decade [*Liu et al.*, 2005; *Schlegel et al.*, 2005; *Carlson*, 2007, 2012; *Demars and Schunk*, 2007; *Rother et al.*, 2007; *Clemmons et al.*, 2008; *Crowley et al.*, 2008, 2010; *Rentz and Lühr*, 2008; *Prölss*, 2010; *Carlson et al.*, 2012; *Sadler et al.*, 2012; *Wilder et al.*, 2012; *Zhang et al.*, 2012; *Deng et al.*, 2013; *Kervalishvili and Lühr*, 2013; *Lühr and Marker*, 2013; *Aruliah et al.*, 2015].

As summarized in *Carlson et al.* [2015], the community has both learned a great deal and made considerable progress, remains short of consensus on significant issues, and has converged to common agreement on enough key points that it is now timely to present new observational data essential to moving forward with improved space weather and even climatological understanding and modeling of the high-latitude thermosphere, for post analysis, specification, and prediction.

Now we must focus on the energy deposition of frictional heating. *Carlson* [1998, 2007] pointed out that the nature of the cusp precipitation made the thermosphere inherently vastly more responsive to energy deposition from reconnection in the cusp than to energy deposition in the nightside auroral region. Heat input increases temperature and thus pressure, expanding the atmosphere upward above the altitude at which heat is injected. In daytime heating by solar radiation, most models assume a base level (isopycnic point) below which the atmosphere is assumed fixed (usually near 100–120 km), above which increasing thermospheric temperature increases density at all altitudes. The density decreases by a factor *e* for each scale height (roughly a factor 10 every two scale heights). At high latitudes particle and ion-frictional drag heating (also called Joule heating as well summarized by, e.g., *Thayer and Semeter*, 2004, Appendix A) injects additional heat which as *Thayer and Semeter* [2004] explain must be treated as an *altitude discriminated* heating rate to get the correct answer. For energy deposition at *E* region heights, *Burns et al.* [1989] showed that for auroral (particle) heating peaking around midnight around 110–120 km, the thermosphere responds over hours. While the mesosphere and lower thermosphere are solar radiation dominated as they corotate with the Earth, the cusp thermosphere can dramatically respond to electric fields in ways critically dependent on MLT, especially near MLT noon. *Carlson* [1998] showed that energy deposition (transient ion-frictional drag) peaking within a scale height of 200 km altitude leads to far greater (order of magnitude) and faster (fraction of an hour) thermosphere response. The weight of a column of atmosphere above 110 km is more than 2 orders of magnitude heavier than above 200 km, so it simply takes far less energy injection around ~200 km to uplift the tenuous thermosphere for the cusp situation, than near 110–120 km for the nighttime aurora situation. This was quantified by *Carlson et al.* [2012] and by *Demars and Schunk* [2007] provided one removes the energy input below 180 km (as explained in *Carlson* [2007]).

The bottom line is, as so well summarized in *Thayer and Semeter* [2004], one must specify the incremental altitude band within which each increment of energy is injected. Integral energy deposition summed over large altitude ranges (as so often done for computational convenience) can lead to very large errors in this nonlinear problem area. As quantified in *Carlson et al.* [2012], in the cusp the electron density profile ($N_e(h)$) puts most of the ion-frictional drag (or alternately said, Joule heating) in the upper thermosphere at altitudes where it is most effective at producing density enhancements by upward thermal expansion. How intense the heating is depends on the square of the plasma drift speed relative to the neutral rest frame (i.e., difference of the horizontal plasma speed versus the neutrals, or horizontal $(\Delta V)^2$). Plasma flow jets up to 2–3 km/s produce 10–30 times the heating rate one would get using standard models with shears of 0.5–1 km/s. The inability to measure satellite drag on scales of degrees of latitude versus fraction of an orbit left this

"should happen" physics untested. *Lühr et al.* [2004], with their state of the art high spatial resolution satellite drag data, were first to publish experimental proof of the major difference, which thermosphere density and drag up to doubled over the cusp but nowhere else over the auroral region. This motivates our need for realistic statistics on $N_e(h)$ and ΔV or equivalently $T_i - T_n$.

The heat driving this upwelling is largely Joule heating, magnetic reconnection is intimately involved, and soft particles steer the heat input to where it has the greatest impact.

Using equations (1)–(3) of *Carlson et al.* [2012] (the equivalence of which was demonstrated in Appendix A of *Thayer and Semeter* [2004]) translates this physics into a linear dependence on electron density (N_e) below ~200 km, and a square law dependence on the ion-neutral velocity shear ($V_i - V_n$). That the neutral density at 200 km is about 10 times more tenuous than at 150 km makes the thermosphere significantly more responsive to heat input in the 175–200 km range than 150–175 km.

In short, the neutral density/drag enhancement near 400 km depends sensitively on (1) the frequency of occurrence of magnetic reconnection events in the cusp; (2) the magnitude of the flow shear ($V_i - V_n$) in these reconnection flow jets, or equivalently the ion temperature enhancement ($T_i - T_n$); and (3) the $N_e(h)$ enhancement near and below ~200 km due to precipitation enhancements at the feet of newly opened magnetic flux tubes at the onset of these reconnection events.

Our knowledge of each of these three parameters is anecdotal. *Carlson* [2012] has summarized what is known of these, for guideline values, with examples, and put these in the context of cusp and overall thermosphere heating. However, no systematic statistical study of this has ever been done; hence, filling this void is the purpose of this paper. To this end, we will (1) present statistics of how often enhanced ion temperatures occur in the dark cusp region and then (2) present representative statistical profiles of cusp electron density and ion temperature, both for the case that the cusp is quiescent and that the cusp is enhanced by ongoing reconnection.

We organize this paper as follows: Section 2 summarizes the equations of plasma heating and thermospheric energy deposition, followed by a description of the incoherent scatter radar and supporting optical data, and the signatures of the cusp seen by these instruments. Section 3 describes and discusses statistical T_i and N_e profiles from EISCAT Svalbard Radar (ESR) field-aligned data to be used as input to calculate model profiles of energy deposition rates in the cusp. Section 4.1 discusses maximum T_i occurrence rates from ESR scanning mode covering a larger area of the cusp. Section 5 presents a summary and conclusions.

2. Methodology

2.1. Background

To bring readers with diverse backgrounds to common ground, for application of the measurement techniques underlying this work, we review a few essential points. We follow the work of *Thayer and Semeter* [2004], using the formulation and terminology in their Table 1. Their height-resolved Joule heating rate ($\mu W/m^3$) can be derived from three mathematically equivalent formulas:

$$\vec{j} \cdot \vec{E}'; \sigma_p E'^2 \tag{1}$$

$$\frac{\delta E_n}{\delta t} = \sum_i n_i m_i \nu_{in} \left(\vec{V}_i - \vec{V}_n \right)^2 \tag{2}$$

$$\frac{\delta E_n}{\delta t} = \frac{3k_B}{m_n} \sum_i n_i m_i \nu_{in} \left(T_i - T_n \right) \tag{3}$$

where E' is the electric field in the neutral rest frame and E_n is the internal energy of the neutral gas. As noted and applied in *Carlson et al.* [2012], the data to be used determines which of these three formulations can be most usefully applied. Here we do not measure the neutral wind field rest frame, and so cannot use equation (1) or (2). We use equation (3), measuring T_i in the relevant altitude range, with statistical error bars and time resolution suited to deriving the heat exchange rate. Reconnection events span ~5–20 min while the ion frictional drag heating and cooling rates of the ion gas come to equilibrium in order 1–2 min. Our interpulse period of ~10 ms gives us a sampling rate of ~100 altitude profiles per second, and we integrate measured $T_i(h)$ with 0.5–1 min time resolution (raw statistics near a little over one percent), to derive heating rates, etc. *Strangeway* [2012] shows why the theory of the physics may best be considered in terms of ion frictional drag heating.

This scatter of the measured value of N_e or T_i is due to both random statistical (Gaussian) error bars in the measurement technique itself (order <10%), but with additional variability due to time dependent geophysics-driven enhancements. The latter physics-driven perturbations are far larger, approximately thousands of kelvins. Where N_e is too low, the incoherent scatter radar (ISR) signal becomes too weak to give acceptable error bars (>25%); we avoid any such problem above ~170 km by adopting an ~400 km cutoff altitude for our study. There are rare data dropouts around 150 km due to very low N_e and thus very weak signal, but whenever there is soft cusp electron precipitation, that precipitation itself always insures sufficient N_e for good ISR data. This occasional data dropout near 150 km thus is only relevant to data outside the cusp.

Different measured geophysical parameters appear with different time delays, as detailed in *Carlson et al.* [2004, 2006]. Onset of reconnection at the magnetopause triggers a sequence of effects. It immediately opens a flux tube, precipitating an immediate pulse of soft cusp precipitation. The N_e much below 200 km closely tracks (order of seconds) the magnitude of this precipitation flux, 557.7 nm emission starts within ~3/4 s, and the 630.0 nm emission immediately begins to rise but with a peak response delayed ~100 s near ~300 km, but as collisional quenching increasingly deactivates emissions at ever lower altitudes, the effective emission lifetime decreases to ~30–40 s approaching 200 km. Electrons heat with ~30 s response time, starting with the precipitating flux onset. In contrast it takes ~2 min at the Alfvén speed for the electric field to start moving the ions (velocity V_i), after which in turn frictional heating builds up T_i with a response time on order a few seconds at 200 km altitude and order 10 s at 350 km altitude. V_i is taken in the *F* region, but we model the height dependence as it twists deeper into the *E* region. Note that while the electron precipitation is almost immediate (delay equal to electron flight time from magnetopause to ionosphere, order of 10 s), it carries a field-aligned current, and the plasma flow is considered the convection equivalent of the DP 2 current system, it takes a finite time for the associated *E* field to communicate itself from the magnetopause to move the *F* region ionosphere, and this Alfvén speed delay is generally considered to be order 2 min, as detailed, e.g., in *Lockwood and Cowley* [1988].

2.2. Frictional Energy Deposition Estimates

Ion frictional heating in the ionosphere can to a good approximation [e.g., *St.-Maurice and Hanson*, 1982] be described as

$$m_n \left|\vec{V}_i - \vec{V}_n\right|^2 \approx 3k_B \left(T_i - T_n\right) \tag{4}$$

where subscript *n* refers to neutral species and subscript *i* refers to the ion gas. k_B is Boltzmann's constant, m_n is the neutral molecular mass, and $\vec{V}_i$ and $\vec{V}_n$ are the ion and neutral velocity vectors. We assume in this paper that T_i and $\vec{V}_i$ are the same for all ion species.

Figure 1a illustrates the square law dependence of T_i on velocity shear for ion-neutral frictional heating, for three different altitudes and different T_n. Since the neutral density greatly exceeds the ion density, T_n responds more than 1000 times more sluggishly than T_i, whence for these time scales $\lesssim$15 min we take any change in neutral temperature to be negligible relative to the T_i change. The variation in the value of $T_i - T_n$ is thus predominantly the variation in T_i. Similarly, we assume that $\vec{V}_n$ does not change appreciably in 15 min, and the variation in T_i is driven by the variation in $\vec{V}_i$.

The altitude variation is due to the differences in molecular composition of the thermosphere, which changes the mean molecular mass. The figure uses the Mass Spectrometer Incoherent Scatter (MSIS)-E-90 model composition for 22 January 2012, 0800 UT above the ESR. At 150 km altitude, the composition is 58% N_2, 6% O_2, and 35% O, which works out to a mean molecular mass of 24 atomic mass units (AMU). At 200 km the composition is 40% N_2, 3% O_2, 57% O, and $m_n = 21$ AMU. At 350 km the composition is 7% N_2, 0% O_2, 87% O, and 5% He, and $m_n = 16$ AMU. It follows from equation (4) that as the mean molecular mass drops with altitude so does the ion frictional heating for a given flow shear velocity. Using MSIS composition from other winter days used in this paper changes the computed T_i by 2–10% for a flow shear of 3000 m/s, less for lower velocities.

Thayer and Semeter [2004] presented equations to estimate the energy deposition rates in the neutral thermosphere from the convergence of electromagnetic energy. They show that for the ionosphere, one can use equation (5) for the rate of energy deposition to a neutral species (in units W/m^3):

$$\frac{\delta E_n}{\delta t} = \frac{3k_B}{m_n} \sum_i n_i m_i \nu_{in} \left(T_i - T_n\right) \tag{5}$$

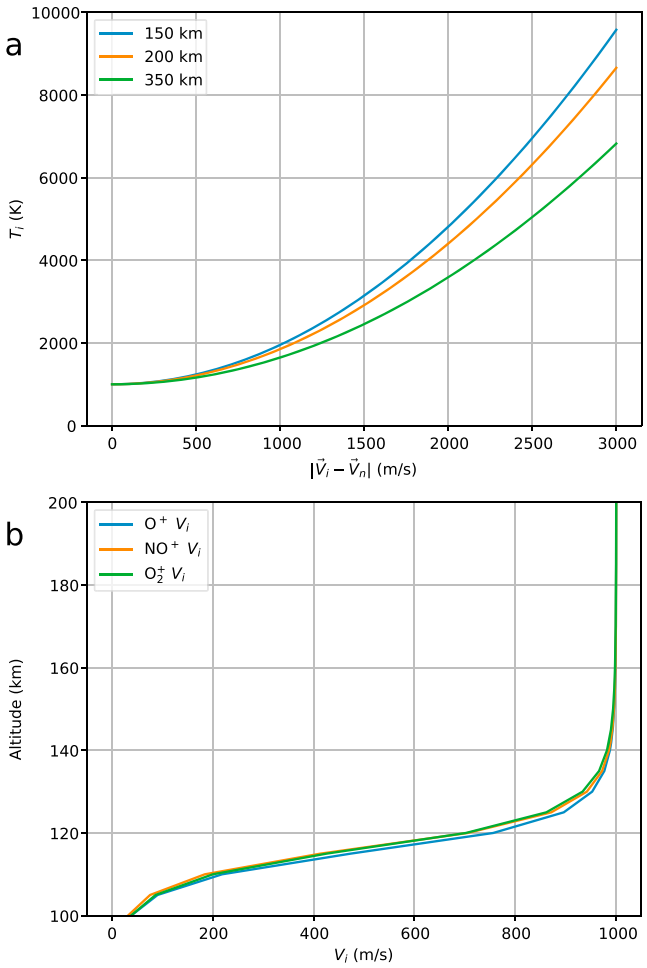

Figure 1. (a) Relationship of ion temperature to ion-neutral velocity shear following equation (4) for 150, 200, 350 km altitude, assuming T_n = 1000 K. (b) Model altitude variation of V_i magnitude for *F* region V_i = 1000 m/s for the main ion species. Atmospheric composition is taken from MSIS-E-90 and International Reference Ionosphere 2012 (IRI2012) above the ESR for 22 January 2012 at 08:00 UT.

where n_i is the ion species number density and ν_{in} is the ion-neutral collision frequency. We use collision frequencies from *Schunk and Nagy* 2009, pp. 105–107].

Equivalently, using the relationship between plasma temperature enhancement and ion velocity shear in equation (4), one can use:

$$\frac{\delta E_n}{\delta t} = \sum_i n_i m_i \nu_{in} \left| \vec{V}_i - \vec{V}_n \right|^2 \tag{6}$$

In the *F* region the ion motion is dominated by the $\vec{E} \times \vec{B}$ drift, but in the *E* region the collision frequency is on the order of the ion gyrofrequency and $\vec{V}_i$ is rotated in the direction of the neutral wind and diminished in magnitude. This effect is approximately equal for all relevant ion species and is described by equations (7) and (8) [e.g., *Rishbeth and Garriott*, 1969]:

$$\tan \theta_i = \frac{\omega_i}{\nu_{in}} \tag{7}$$

$$V_i = \frac{E}{B} \sin \theta_i = V_{iF} \sin \theta_i \tag{8}$$

where θ_i is the angle between the ion velocity vector $\vec{V}_i$ and the electric field $\vec{E}$, ω_i is the ion gyrofrequency, and V_{iF} is the F region $\vec{E} \times \vec{B}$ velocity magnitude. Figure 1b shows this effect on the magnitude of V_i modeled

for $V_{iF} = 1000$ m/s. The heating rates presented later in this paper use the average of the three ion velocity profiles shown.

For brevity we write ΔV instead of $\left|\vec{V}_i - \vec{V}_n\right|$ for ion-neutral flow shears from now on.

2.3. Optical Data

Optical data come primarily from the University Centre in Svalbard (UNIS) meridional scanning photometer (MSP) at the auroral station (AS) in Adventdalen, 6 km west of ESR, and the Kjell Henriksen Observatory (KHO), colocated with ESR. KHO opened in 2008 and took over the instruments from AS. Optical data from the University of Oslo MSP and all-sky cameras at the Sverdrup station in Ny-Ålesund, 120 km NE of ESR, were also used if available.

Optical overview data were used when available to assist in identifying time intervals when the field-aligned radar beam was in or near the cusp aurora.

2.4. EISCAT Svalbard Radar

The data examined in this paper are produced by the European Incoherent Scatter (EISCAT) Svalbard Radar (ESR) [*Wannberg et al.*, 1997; *Grydeland et al.*, 2004]. The ESR is an incoherent scatter radar located at 78.15°N, 16.03°E, 12 km east of Longyearbyen, Norway. It has one steerable 32 m dish (operational 1996) and one 42 m dish (operational 1999) fixed pointing parallel to the geomagnetic field in the *F* region.

The Altitude-Adjusted Corrected Geomagnetic coordinates (AACGM v2) [*Shepherd*, 2014] for ESR were 75.02°N, 111.80°E in 1998, and 75.34°N, 109.59°E in 2012. The drift in geomagnetic coordinates follows the drift of the International Geomagnetic Reference Field (IGRF) geomagnetic model field [*Thébault et al.*, 2015].

Two radar modes were used. One is the field-aligned mode where the radar beam is directed parallel to the *F* region geomagnetic field. All the plasma in the beam at any given instant is then approximately in the same flux tube and subject to approximately the same magnetospheric/solar wind input. The fixed position field-aligned mode allows measurements with high resolution in altitude in the *E* and lower *F* region, crucial when modeling the thermospheric response [*Carlson et al.*, 2012; *Aruliah et al.*, 2015]. The data we use have an integration time of 60 s. A disadvantage of the longer integration time is that the plasma in the beam is continuously moving horizontally, so the integration will average over all the plasma which passes through the beam during the integration period.

The other radar mode is a scanning mode first described by *Carlson et al.* [2002], where the radar is moved continuously while transmitting. Two scanning submodes were used:

1. One is the elevation scan mode, with the azimuth held constant and the radar scanning from 30° to 150° elevation. The radar beam sweeps a circle sector, with the sweep plane aligned toward geomagnetic north (roughly 30° west of geographic north).
2. The other one is the azimuth scan mode, where the elevation is held constant at 30° and the radar scans 120° in azimuth, sweeping the beam along a conic surface.

The elevation scans used for this paper have a duration of 128 s, and azimuth scans 192 s.

This scanning allows mapping temperatures, plasma density, and line-of-sight velocities over a large area with a high rate of repetition (2–4 min), at the cost of large statistical error bars, since only short integration times are possible when good spatial resolution and rapid beam movement are desired. The scanning data use an integration time of 3.2 s, which nonetheless measures real temperature enhancements order of thousands of kelvins with error bars down to an order of magnitude smaller. The beam was scanned toward the sector where the cusp was most likely to be, i.e., before noon MLT the radar was scanned in azimuth scanning mode toward the eastern sector, near noon when the cusp was likely overhead the elevation scan mode was used, and after noon MLT the azimuth scanning mode was again used, this time in the direction of the west-southwest sector.

Some terminology: When the radar is moving in the scanning mode, we refer to one sweep from start to end as a "scan." The data can be naturally divided into scans, since they have a well-defined start and stop. When the radar is static field aligned, the time resolution is set by the integration time of the return signal in the analysis. We will refer to the output of one integration as one "measurement." Each measurement contains the four basic parameters N_e, T_e, T_i, and V_i along the line of sight. In this paper we reserve the word "profile" for average and median altitude profiles computed from many radar measurements.

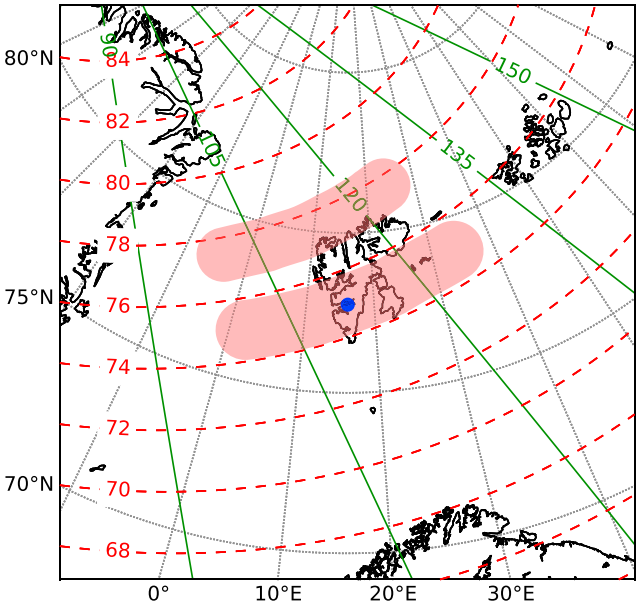

Figure 2. Schematic illustration of the cusp at magnetic noon located overhead (lower red blob) Svalbard and poleward (upper red blob) of Svalbard, projected to 250 km altitude. The cusp is drawn to cover approximately 2° in magnetic latitude and 45° in magnetic longitude (3 h magnetic time), corresponding to the statistical width of the cusp proper [*Newell and Meng*, 1992; *Newell et al.*, 2004]. Green lines show MLON, drawn 15° (1 h) apart. Dashed red lines show MLAT. The blue marker shows the location of the ESR field-aligned beam at 250 km altitude (field of view not to scale).

2.5. Definition of the Cusp and Identifying When the Radar Beam Is in the Cusp

Since we wish to examine energy deposition in the cusp, we need to define the cusp as seen from the ground. *Newell and Meng* [1988] originally divided the dayside magnetosheath precipitation into two morphological regions, cusp and the low-latitude boundary layer (LLBL). The distinction was attributed to a step in the magnetosheath ion energy spectra. *Smith et al.* [1992] and *Cowley et al.* [1991] predicted a staircase ion energy signature due to transient magnetopause reconnection, which was experimentally verified by *Yeoman et al.* [1997]. In the *Newell and Meng* [1992] probability map, the cusp spans from 10:30 to 13:30 magnetic local time (MLT) (3 h). The LLBL footprint in the ionosphere, also referred to as the cleft, borders on the equatorward side of the cusp near noon but spans from ~09:00 to 15:00 MLT (6 h). Optically, the cusp and LLBL regions are not expected to be separable from each other in the auroral emissions, since there is no corresponding cusp/LLBL energy step in the electron precipitation [*Moen et al.*, 1998]. The cusp/cleft aurora contains the poleward moving auroral forms (PMAFs), classified as Type 1 aurora by *Sandholt et al.* [1998], that have plausibly been attributed to ~100 eV magnetosheath electron precipitation on open field line [*Moen et al.*, 1996, 1998; *Oksavik et al.*, 2000]. The low initial energy of the precipitating electrons favors excitation above 200 km altitude, where the red auroral emission is not strongly quenched by collisions. Ground observation of continuous cusp/cleft-like optical emission spanning ~90° of longitude or 5 h MLT has been reported [*Valladares et al.*, 2002].

On average, the cusp is centered on 12 MLT. However, negative (positive) IMF B_Y can shift the cusp prenoon (postnoon) in the Northern Hemisphere, and opposite for the Southern Hemisphere [*Newell and Meng*, 1989; *Moen et al.*, 1999]. The north-south location of the cusp varies with the size of the polar cap, which can change rapidly when dayside and nightside reconnection rates differ [*Cowley and Lockwood*, 1992; *Lockwood et al.*, 1993; *Moen et al.*, 2004a]. Figure 2 illustrates schematically how the north-south position of the cusp can vary. The cusp is drawn as a region covering 2° in magnetic latitude (MLAT) and 45° wide in magnetic longitude (MLON) (3 h magnetic time), corresponding to the statistical width of the cusp proper as defined by *Newell and Meng* [1992]; *Newell et al.* [2004], and half the width of the statistical cusp/cleft region. The north-south positions of the cusp shown in the figure correspond to the maximum north-south motion of the cusp/cleft aurora observed on 20 December 1998 [*Moen et al.*, 2004b]. However, since the electron precipitation in the cusp proper and the cleft is very similar, the signatures of both regions in both optical sensors and incoherent scatter (IS) radar will be similar in the two regions. As we are not able to distinguish between cusp and cleft from ground based data, we refer to this region as cusp in the rest of this paper.

Since the geomagnetic pole in the northern hemisphere is located in northern Canada, the cusp is closer to the geographic north pole in the European sector than in the American sector. The ionospheric cusp when over Svalbard is close to the geographic pole (76° – 80° geographic latitude). Near midwinter, the Earth's axial tilt brings this region well into the Earth's shadow even at local noon. Thus, there will be no significant photoionization in the *E* region and lower *F* region. This ionospheric cusp without local photoionization is also called "dark cusp". Below ~200 km recombination is rapid enough that any observed ionization must be

produced where it is observed; as it is observed, *Walker et al.* [1999] found that an enhanced structure of 4 times background N_e at 200 km would decay to 2 times background in ~40 s. Transport of plasma patches can only occur at higher altitudes. By restricting this study to data from the dark cusp, we can assume all ionization in the *E* region to be due to precipitation and use the absence of an *E* layer around 100–120 km which would be produced by keV precipitation and a corresponding increase of background N_e around 150–250 km altitude from ~200 eV precipitation as an indication of soft precipitation on dayside open field lines. Minimal N_e below ~150 km demonstrates the absence of hard particle flux; enhanced N_e above 150 km but in the lower F region demonstrates the presence of soft particles. Ionization much above 200 km has such a long chemical lifetime that it need not be produced locally but could be transported large horizontal distances.

To summarize: The primary diagnostic for determination of cusp is (1) by optics: a sudden increase in ratio of intensity of 630.0 nm to 557.7 nm (or 427.8 nm) indicating an increase in the ratio of soft to hard particle fluxes [*Lorentzen and Moen*, 2000] and/or (2) by field-aligned IS radar: increase in electron density near 150–250 km [*Moen et al.*, 2001] coincident with decrease in electron density near 110–130 km. In addition, we expect to see reconnection signatures some of the time.

2.6. Radar Signature of Reconnection

We now need to define criteria for identifying energy deposition, i.e., a radar signature of reconnection. The ionospheric signature of a dayside reconnection event is described in detail by *Carlson et al.* [2004, 2006], and we briefly summarize it here. The precipitating cusp electrons will rapidly heat the electron gas throughout the flux tube they traverse, down to near ~150 km altitude, and ionize the thermosphere, increasing the electron density around 150–250 km altitude. Increased T_e also expands N_e upward [*Skjæveland et al.*, 2011]. The penetration depth is controlled by the initial electron energy [*Kamiyama*, 1967; *Moen et al.*, 2001]. Onset of reconnection is manifested by an optical flash (prompt for 557.7 nm, starting to rise immediately but with peak response delayed order of a minute for 630.0 nm), lasting several minutes, while the newly opened flux tube is drained of order 0.1–1 keV electrons. Subsequent parameter signatures follow as given in *Carlson et al.* [2004, 2006]. The electron density production is enhanced below 200 km by the same ionizing electron precipitation that produces the impact-excited optical emissions. The 557.7 nm emission peaks within a second, while the 630.0 nm emissions are ramping up more slowly. A channel of enhanced plasma flow in the ionosphere starts with a delay of ~2 min as the reconnection electric field maps down from the magnetopause, producing coincident frictional drag heating of the ions. The optical signature is located on one flank of the flow channel [*Oksavik et al.*, 2004, *Oksavik et al.*, 2004, 2005; *Moen et al.*, 2008, 2012] and is visible for 5–8 min [*Sandholt et al.*, 1989, 1998]. The flow channel is of typical duration ~15 min, which is sufficient time for the frictional drag heating to accumulate measurable thermospheric heating above ~175 km [*Carlson et al.*, 2012]. The flow channels have an azimuthal and poleward component, where in principle if the IMF B_Y were zero, the flow would be poleward, but strong shear flows (and upflows) are associated with larger B_Y components. Here one can crudely think of the flows as more L shell aligned, with observed lifetimes of 15–20 min, and a length exceeding 1000 km. The flow channel can be thought of as in response to the reconnection flux tube reconfiguration, with a magnetic tension force driving the reconnected magnetic flux tube westward (eastward) in the Northern Hemisphere for IMF $B_Y > 0$ (<0), and with a poleward component of motion for IMF southward. This motion can be seen optically as a PMAF.

The signature of cusp defined above does not distinguish clearly between cusp and dayside polar cap. The reconnection-driven flow channels and the associated auroras have been observed to drift into the polar cap while still active, as observed by optical [e.g., *Fasel*, 1995, and references therein] and radar studies [*Oksavik et al.*, 2004; *Rinne et al.*, 2007, 2010]. These events may still be producing heat and upwelling in the near polar cap. Since this paper aims to study the ionospheric processes causing thermospheric upwelling, it is not necessary for our purposes to define a clear poleward boundary of the cusp. It is also worth noting that it is rare for the polar cap to expand so much that the ESR field-aligned beam is well within the dayside polar cap. This is most likely for *Kp* values of 5 or more, which is not the case for our chosen data.

The next item to clarify is the radar signature of these reconnection events. For the ESR in a geomagnetic field-aligned static beam configuration, the field of view is narrow and the radar view of the ionospheric reconnection signature is limited. The increased electron precipitation will manifest as increased electron density and temperature, and the flow channel will be seen as an increase in ion temperature. The flow channel is not normally observable in the line-of-sight (LOS) ion velocity (V_i) data, as the horizontal component contribution to the LOS V_i will be small and probably dwarfed by ion upflow [*Skjæveland et al.*, 2011]. The reconnection

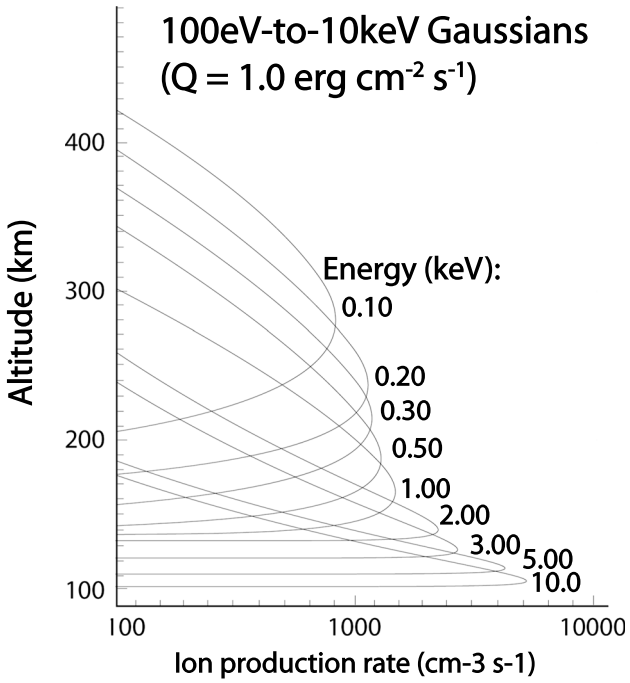

Figure 3. Ion production rate profiles for different precipitating electron energies for the same energy flux. From *Carlson et al.* [2012].

foot point will convect along with the large-scale polar cap convection, and this convection limits how long the event is observable by the radar.

The initial precipitation arrives before the reconnection electric field creating the V_i and T_i enhancements has mapped fully down into the ionosphere (~2 min delay). The horizontal scale of the N_e and T_i signatures is such that they will both be visible for 2–5 min in a field-aligned radar beam as they convect across. Because of the spatial separation between the two enhancements (the maximum T_i will most likely be near the center of the flow channel, while the N_e enhancement will be greatest in the auroral arc, located on the flank of the flow channel), the time offset between the T_i and the N_e enhancement convecting across the radar beam is 0–2 min. However, since the T_i enhancement appears at the ionospheric foot point order 2 min after the N_e enhancement and lasts significantly longer (5–8 min for the N_e enhancement [*Sandholt et al.*, 1998; *Carlson et al.*, 2004] versus 5–19 min for flow channels [*Rinne et al.*, 2007]), the field-aligned, near-vertical radar beam will not necessarily encounter both the T_i and N_e enhancement from the same reconnection event.

Hard auroral particle fluxes penetrate below 100 km; soft cusp fluxes penetrate much less deeply. Figure 3 quantifies this statement between 0.100 and 10.0 keV. For the interested reader, a comparison with actual ESR $N_e(h)$ data flipping between soft cusp versus harder auroral particles can be found in *Carlson et al.* [2012].

The horizontal plasma flow will be fairly constant with altitude above ~150 km. T_i will be enhanced in a structure along the geomagnetic field, from the top of the *E* region through the *F* region, with an altitude variation that can be derived from equation (4) by taking into account the altitude variation of m_n and the collisional quenching of ΔV below 120 km shown in Figure 1b.

We use field-aligned data with high-altitude resolution to compute statistical N_e and T_i profiles. For 20 December 1998 the 32 m dish was pointed field aligned, for later data the fixed 42 m dish was used. Data were collected and analyzed using the standard analysis for each data set. The data were then interpolated and resampled to a 5 km altitude resolution, to avoid problems due to variations in the altitude gating between measurements.

3. Statistical T_i and N_e Profiles From ESR Field-Aligned Data

The energy input in the dark cusp comes mainly from magnetopause reconnection, and it is important to know the typical energy input for accurate modeling. Since the reconnection rate is highly variable, we seek to measure the cusp in two different states: quiescent and reconnection enhanced.

Because the enhancements of N_e and T_i have different lifetimes after magnetopause reconnection and are not quite colocated in the ionosphere, the field-aligned radar beam will not necessarily encounter both signatures from the same event simultaneously but may see them one after the other or even only one of them. For this reason we handle the two enhancements independently. We use N_e to divide the cusp observations into quiescent and enhanced periods based on N_e quiescent/enhanced alone, and independently, we use T_i to divide the cusp observations into periods when T_i is quiescent/enhanced. In the following text we will refer to these two ways of dividing the cusp observations by the shorthands N_e *bimodal* and T_i *bimodal* cusp

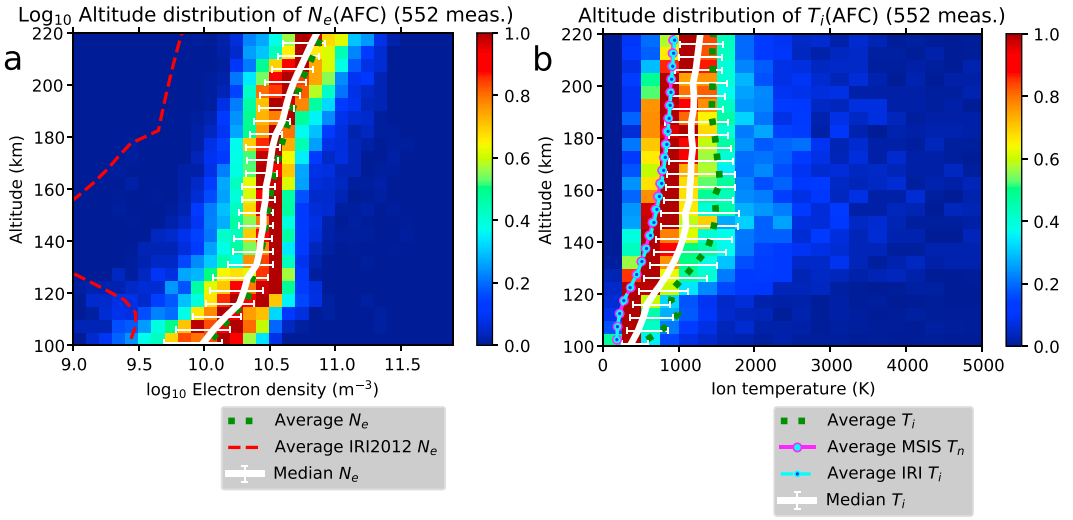

Figure 4. Density histogram of (a) N_e distribution (all cusp data) N_e(AFC), with median and average N_e and average IRI2012 N_e superimposed, and (b) of T_i distribution (all cusp data) T_i(AFC), with median and average T_i, and average MSIS T_n and IRI2012 T_i superimposed. Error bars on median show 25th and 75th percentiles.

observations. We show data and results from 100 to 220 km altitude in the following text. The heating deposition that drives the cusp upwelling occurs mainly between 175 and 200 km, while nightside auroral heating deposition is strongest around 100–120 km.

3.1. Statistical Profiles Using All Field-Aligned Cusp Data

We now proceed to the statistical profiles of T_i and N_e. Figure 4a shows a color plot of the distribution of all the cusp Ne data used in this paper, where each row, corresponding to one altitude gate, is a 1-D histogram of all the observed N_e measurements at that altitude that go into computing the model profiles. The data were resampled to 5 km resolution in altitude to avoid bias from uneven range gates and to get all the data into the same altitude grid. Each row is scaled so that its peak value is 1, i.e., dark red shows the most common N_e at that altitude. Also shown are average IRI2012 [*Bilitza et al.*, 2014] model N_e (dashed red line), the average N_e (dotted green line), and median N_e (white line, with error bars). The error bars show the 25th and 75th percentile of the input data used in averaging at each altitude.

The figure title contains the minutes of radar measurements used to compute the average/median profile. This number is slightly smaller than the amount of available data listed in Table 1, since a few profiles are automatically filtered out from the averaging.

The figure shows N_e in logarithmic scale, while the median, average, and error bars are computed in linear space. The error bars are shown only on the median profile to limit visual cluttering. The average and median N_e profiles track the most common N_e fairly closely.

Table 1. Overview of ESR Field-Aligned Data Used

Date	Total Time in Cusp	T_i Quiescent	T_i Quiescent	N_e Enhanced	N_e Enhanced	*Kp* Index[a] 06–09 UT	*Kp* Index[a] 09–12 UT
20 December 1998	121 min	22 min	99 min	78 min	43 min	3–	3–
24 January 2001	37	16	21	3	34	1	(3+)
27 January 2001	55	24	31	8	47	(1)	1–
28 January 2001	160	71	89	65	95	1+	2–
29 January 2001	97	43	54	19	78	2	1+
22 January 2012	88	6	82	16	72	4+	4–
Total	558	182	376	189	369		

[a] *Kp* in parantheses indicates no data from that period were used.

Figure 4b shows a similar figure for all the T_i data. Also shown are average MSIS-E-90 model [*Hedin*, 1991] neutral temperature (T_n, purple line with cyan dots), average IRI2012 model ion temperature (dashed cyan line, blue dots), the average T_i (dotted green line), and median T_i (white line, with error bars). In all the figures of this type, the IRI2012 T_i is very close to the MSIS T_n in the altitude range shown. The difference is at most 40 K, which almost vanishes in these plots. The model T_n tracks the most common T_i closely. The long tail of the temperature distribution increases the average T_i up to ~1500 K, while the median is around ~1250 K. The error bars again show the 25th and 75th percentile of the input data.

We will show such figures for all the bimodal cusp data sets defined in the next section. For each radar measurement we also computed the MSIS-E-90 T_n and the IRI2012 N_e and T_i. Since these model values vary with time of day and season, we computed average profiles and median profiles of these the same way as for the radar measurements. For all three model data there is no significant difference between the median profile and the average profile. For empirical N_e the average is about 5–15% greater than the median, and for empirical T_i the difference is 15–25%.

The statistical profiles shown in Figures 4a and 4b are based on the complete set of cusp field-aligned data which includes both quiescent and reconnection-enhanced periods, and how often the cusp is quiescent and enhanced will vary from day to day. For modeling of neutral upwelling response to reconnection we will need separate model profiles of reconnection enhanced versus quiescent ionosphere.

3.2. Dividing the Field-Aligned Data Into Quiescent and Reconnection-Enhanced Cusp

We searched the EISCAT database for days with field-aligned radar data for the whole period 07–11 UT (which corresponds to ~10–14 MLT), near solar maximum, with supporting optical data when available. This is the UT time range we have commonly observed cusp and reconnection signatures over Svalbard. This time span is smaller than the expected cusp/cleft which is 6 h MLT wide, to ensure we do not collect nightside data in case of strong east/west shifts of the cusp. Although both ESR data and optical data are plentiful, having both at once is less common and there are perhaps surprisingly few days where the sky is clear, the ESR is running in field-aligned mode, and the Sun and Moon are far enough below the horizon to allow the sensitive MSP and all-sky imaging photometer (ASIP) instruments to run. Table 1 shows an overview of the field-aligned data we used, along with *Kp* index as a measure of geomagnetic activity. *Kp* in parentheses indicates that no data from that period were included in our analysis. This occurred when the radar beam was never inside the cusp in that period.

We desired that all field-aligned radar data used could be verified to be in the cusp, so we only chose days where optical data were available at least part of the time to verify that the field-aligned radar beam was inside the cusp aurora. See *Skjæveland et al.* [2011] for a detailed study of the relationship between the cusp aurora and radar signatures. Optical data were generally only available for part of the radar observation period on a given day, due to weather, bright twilight, moonrise, or technical issues. We then used only the radar signatures defined in sections 2.5 and 2.6 to indicate cusp: weak/absent *E* layer, persistently elevated T_e above 200 km. Intermittent enhancements of N_e at 175–200 km and of T_i (due to flow channels) indicate cusp reconnection. When optical data were available, they were used to see if the radar beam was within the cusp aurora and to verify the use of the radar cusp signatures for when optical data were not available. In general, we found good agreement between radar and optical cusp signatures.

Having identified when the cusp is within the radar field of view, the next step is to identify when the cusp is quiescent and when it is reconnection-enhanced. From minute to minute, the best indicators of reconnection-driven energy input in the field-aligned cusp data are enhanced N_e and enhanced T_i. The enhanced N_e will disappear rapidly through recombination after the particle influx stops, within a minute at 200 km and faster at lower altitudes [*Walker et al.*, 1999]. The longer-lived T_i enhancement will fade when the reconnection electric field mapping into the ionosphere fades, and the flow channels relax and disappear in the large-scale polar flow pattern.

Inspection suggests that $N_e = 10^{10.5} = 3.2 \times 10^{10}$ m^{-3} between 175 and 200 km is a reasonable threshold for quiescent/enhanced N_e. The N_e threshold is evaluated as a median of all data points in this altitude range, so one value per radar measurement. During quiet periods in the cusp N_e was mostly near or below this level, while clear event structures and longer enhanced periods were well above it. For T_i, we found that $T_i \approx 1500$ K similarly served as a useful threshold for dividing T_i measurements into quiescent and reconnection-enhanced. Assuming $T_n = 1000$ K, a T_i of 1500 K at 200 km altitude corresponds to a flow shear ΔV of around

800 m/s. The T_i threshold is not exact, as the periods of enhanced T_i were chosen by manual inspection of overview plots in order to separate genuine enhancements from bad data.

Having defined a threshold, we can define the quiescent and enhanced modes:

QN_e N_e bimodal quiescent – N_e is below the enhancement threshold
EN_e N_e bimodal enhanced – N_e is above the enhancement threshold
QT_i T_i bimodal quiescent – T_i is below the enhancement threshold
ET_i T_i bimodal enhanced – T_i is above the enhancement threshold

In addition, it is useful to consider the whole set of cusp field-aligned data without regard to quiescent/enhanced; we label this set AFC (all field-aligned cusp data) for consistent terminology. For each of these sets we will compute statistical profiles of T_i and N_e. We will label these profiles as follows:

N_e(AFC) and T_i(AFC) : Statistical N_e and T_i computed from the "all cusp data" data set.
$N_e(QN_e)$ and $T_i(QN_e)$: Statistical N_e and T_i computed from the N_e bimodal quiescent data set.
$N_e(EN_e)$ and $T_i(EN_e)$: Statistical N_e and T_i computed from the N_e bimodal enhanced data set.
$N_e(QT_i)$ and $T_i(QT_i)$: Statistical N_e and T_i computed from the T_i bimodal quiescent data set.
$N_e(ET_i)$ and $T_i(ET_i)$: Statistical N_e and T_i computed from the T_i bimodal enhanced data set.

We emphasize the median when computing profiles in this paper since it is less sensitive to outliers than the average, and the radar analysis can occasionally give results that are mathematically possible but physically implausible or impossible, such as extreme or negative temperatures. However, we will also show the average values, since averages are most sensitive to extreme high values, and extrema of N_e or T_i naturally result in large energy deposition rates.

3.3. Statistical Profiles for N_e Bimodal Cusp

Figure 5 shows data for the N_e bimodal cusp. Figures 5a and 5b show quiescent data (QN_e); Figures 5c and 5d show reconnection-enhanced data (EN_e). Figures 5a and 5c show N_e; Figures 5b and 5d show T_i.

We will do a quantitative comparison of the various quiescent and enhanced profiles after we have presented all the profiles. Some qualitative observations are as follows: The difference between median and average N_e is fairly small. The average N_e profile is around 105% of the median N_e profile around 175 km altitude for the quiescent case, and 115% for the enhanced case. The spread in the N_e data at 120–160 km is significantly greater for quiescent ($N_e(QN_e)$, Figure 5a, than for enhanced ($N_e(EN_e)$, Figure 5c. The most common T_i is slightly higher for the enhanced case ($T_i(EN_e)$, Figure 5d, than the quiescent case ($T_i(QN_e)$, Figure 5b, which is close to MSIS T_n. The median of $T_i(QN_e)$ is not significantly different from the median of $T_i(EN_e)$, and likewise for the averages. The average T_i is ~250 K higher than the median in both cases.

Figure 6 shows a histogram of N_e values for AFC. Each radar measurement contributes to the histogram an N_e value that is the median of the measured N_e in the range 175–200 km altitude. The vertical red dashed line marks the separating line between quiescent and enhanced N_e for the N_e bimodal cusp. Also marked are the altitude median of the $N_e(QN_e)$ and $N_e(EN_e)$ statistical median profiles in the same altitude range.

3.4. Statistical Profiles for T_i Bimodal Cusp

Figure 7 shows data for the T_i bimodal cusp, in the same arrangement as Figure 5. Here there is little difference between quiescent and enhanced N_e. Average and median quiescent T_i both track MSIS T_n and most common T_i quite well above 150 km. For enhanced T_i, the most common T_i and the median T_i are both close to the threshold of ~1500 K, while the average again is somewhat higher.

We can elaborate further on the chosen threshold values. Reconnection events are studied by observing/tracking sharp boundaries: in time (data staring in fixed directions) or in space (sweeping the radar beam back and forth more rapidly across a boundary than the boundary moves). Observations show almost square wave leaps up/down: of high/low N_e below an altitude of ~200 km driven by crossings of soft particle precipitation boundaries (e.g., Figure 3) and of T_i from low ~1000–1500 K to high ~2000–4000 K values (e.g., Figure 1c of *Carlson et al.* [2012]). This study went beyond the several such anecdotal published examples, to do a systematic study of years of data. We have suggested nominal breakpoints from low to high and should present relevant evidence for the numbers.

T_i is most directly linked to the physics of *Carlson et al.* [2012]. Ion frictional heating is driven by the square law dependence of T_i on plasma flow channels of horizontal ΔV. The heating is significant for flow shears in

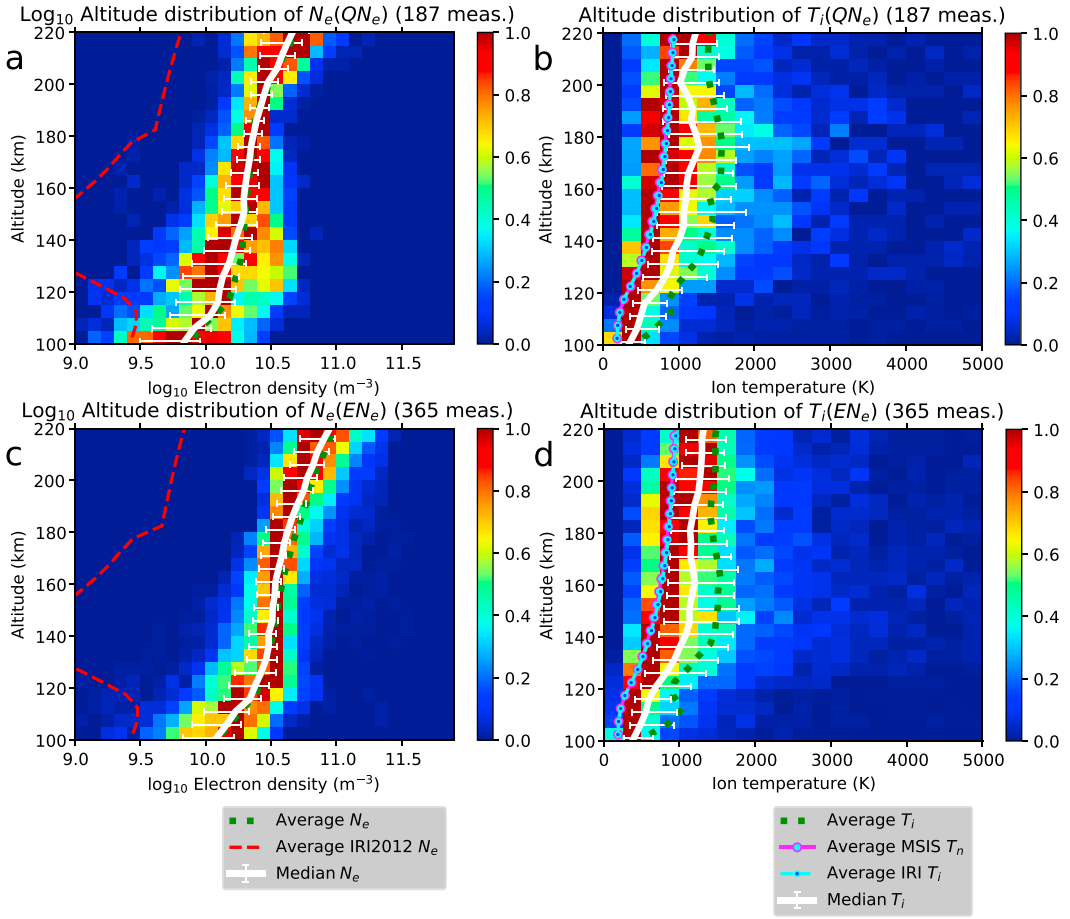

Figure 5. N_e bimodal cusp N_e and T_i density histograms. (a and b) Data for quiescent QN_e; (c and d) enhanced EN_e. Figures 5a and 5c show N_e; Figure 5b and 5d show T_i. Median and average profiles superimposed, and IRI2012 N_e (MSIS T_n, IRI2012 T_i) superimposed on Figures 5a and 5c (Figures 5b and 5d). Error bars on median show 25th and 75th percentiles.

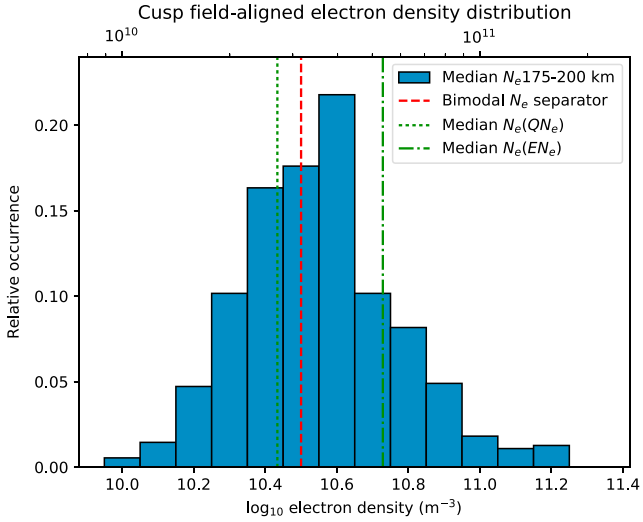

Figure 6. Histogram of N_e median distribution (all cusp data), 175–200 km altitude. Also shown is the separator between quiescent and enhanced states for the N_e bimodal cusp, and the median of the $N_e(QN_e)$ and $N_e(EN_e)$ model profiles in the same altitude range.

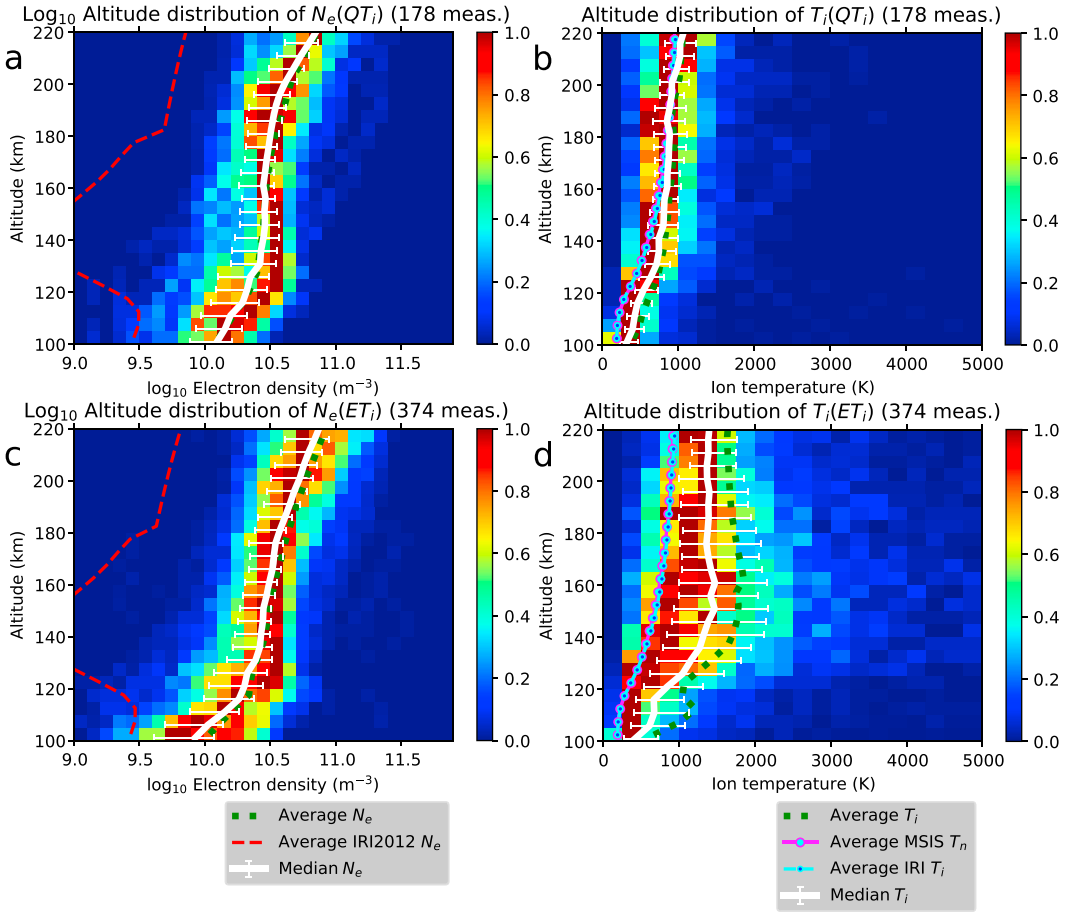

Figure 7. T_i bimodal cusp N_e and T_i density histograms. (a and b) Data for quiescent QT_i; (c and d) enhanced ET_i. Figures 7a and 7c show N_e; Figures 7b and 7d show T_i. Median and average profiles superimposed, and IRI2012 N_e (MSIS T_n, IRI2012 T_i) superimposed on Figures 7a and 7c (Figures 7b and 7d). Error bars on median show 25th and 75th percentiles.

the 1.5–3 km/s range, insignificant in the 0.5–1 km/s range. Figure 1 of *Carlson et al.* [2012] has shown for a single day, a square wave behavior of F region T_i. Of the 40 min of data, there are three 4–6 min periods when $T_i > 2000$ K, and the remaining 24 min T_i is well below that temperature; the times of high T_i coincide closely with all other reconnection signatures. The T_i behavior for our much larger database here is shown in our Figure 7 here, where the median and average T_i for quiet times are nearly equal (within ~50K) to each other at ~1000 K, and equally close to the MSIS value above 180 km altitude. In sharp contrast, for times associated with reconnection events, the average value is well above 1500 K, and even the median T_i is about 1500 K. The data suggest a switch, which we have called on/off at about 1500 K.

Now consider $N_e(h)$. Figure 1 of *Carlson et al.* [2012] shows two profiles typical of time during reconnection events where $\log_{10} N_e(h < 200$ km) exceeds 10.5 and one example typical of N_e during times in absence of reconnection, where $\log_{10} N_e$ is well below 10.5. Figure 5 illustrates the difference between quiescent and enhanced times for the entire data set used herein. The left half of Figure 5 shows $N_e(h)$, with Figure 5a for quiet times and Figure 5c for reconnection-enhanced times. The contrast is striking. All the reconnection time $N_e(h)$ are consistently greater than nonreconnection periods, with nonoverlapping quartile error bars between 160–200 km.

We should point out that our Figures 5 and 7 are based on the identical database and differ only in the criterion for which minutes of data were sorted into which bin (reconnection or not reconnection). Our candidate mechanism [*Carlson et al.*, 2012] separates T_i from N_e effects by temporal and spatial decoupling. The heating effect is significant only for $\Delta V \sim 2$–3 km/s by the square law dependence. Therefore, this mechanism would delay the T_i heating effect ~3 min behind the N_e enhancement onset, and at 2–3 km/s, in 3 min a flux tube can go 360–540 km. Since flow channels are a few 100 km wide, good correlations in one parameter in

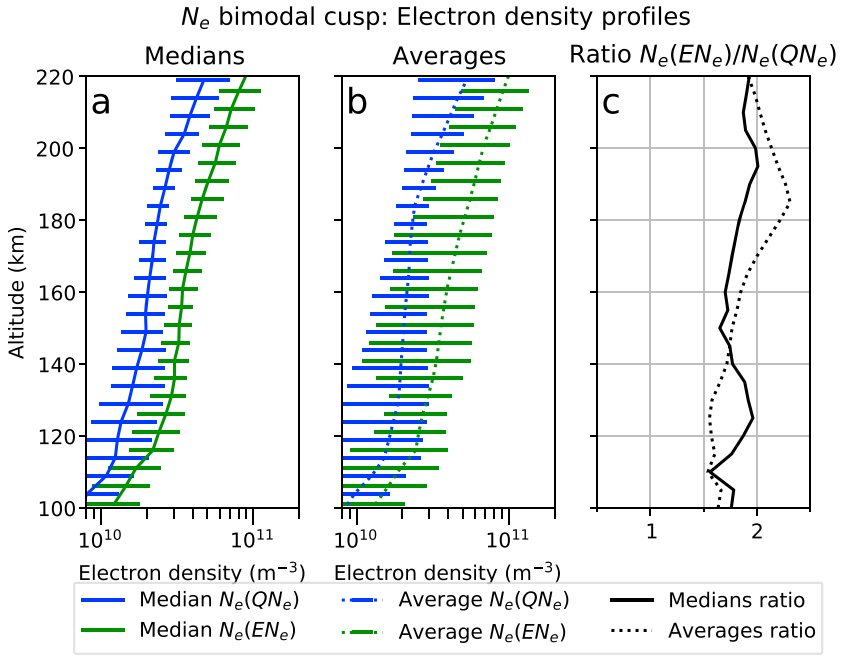

Figure 8. N_e bimodal cusp: Comparison of median and average quiescent and reconnection-enhanced N_e. (a) Error bars show 25th and 75th percentile. (b) Error bars show one standard deviation of input data.

Figure 5 or 7 do not equate to good correlations for the other parameter. One must consider the physics in order to know what correlations to expect.

3.5. Comparison of N_e Bimodal Profiles and T_i Bimodal Profiles

Having established several different statistical profiles, the next step is to compare them to each other.

First, we look at the N_e bimodal cusp. Figure 8 shows a comparison of the N_e profiles for N_e bimodal cusp. Figure 8a shows the median profiles $N_e(\mathrm{QN}_e)$ and $N_e(\mathrm{EN}_e)$. The profiles are offset slightly in altitude so that their error bars do not obscure each other. The error bars show 25th and 75th percentiles of the data used to compute the profile. Figure 8b shows the same, but for the average profiles. Here the error bars show one standard deviation of the input data. Figure 8c shows the ratio of enhanced to quiescent profile. The solid line is the ratio of the median profiles, and the dashed line is the ratio of the average profiles. The enhanced and quiescent profiles in Figure 8a are well separated above ~150 km altitude, with nonoverlapping error bars up to 210 km. Below this altitude range the error bars increasingly overlap, and we cannot consider them distinct at the lower altitudes. The average profiles in Figure 8b are not well separated. The greatest separation and smallest error bars occur around 190 km, but there is still some overlap of the error bars. In the lower and topmost altitudes the overlap is significant, and the enhanced and quiescent average profiles are not distinct from each other. The medians ratio is around 1.6–2.0 between 175 and 200 km altitude, and the averages ratio is 2.1–2.3.

Figure 9 shows a similar comparison of T_i profiles for N_e bimodal cusp. Here the quiescent and enhanced profiles are very similar, with large error bars for both the median and average profiles. The ratios are close to unity, and in view of the large error bars the deviation from unity cannot be considered physically meaningful.

Next, we look at the T_i bimodal cusp. Figure 10 shows the N_e profiles for the T_i bimodal cusp. There is some difference between the quiescent and enhanced profiles both for the medians and averages, but the error bars are large relative to the difference between the two profiles. Both the medians ratio and the averages ratio are 1.2–1.3 at 175–200 km altitude, but given the large error bars relative to the difference between quiescent and enhanced, it is clear that the quiescent and enhanced profiles are not statistically different.

Finally, Figure 11 shows T_i profiles for the T_i bimodal cusp. The quiescent profiles have smaller error bars than the enhanced profiles. The median profiles here are well separated, and the large error bars on the enhanced profiles is partly due to the long tail on the $T_i(\mathrm{ET}_i)$ distribution. The medians ratio is 1.5–1.6, and the averages ratio is 1.6–1.8.

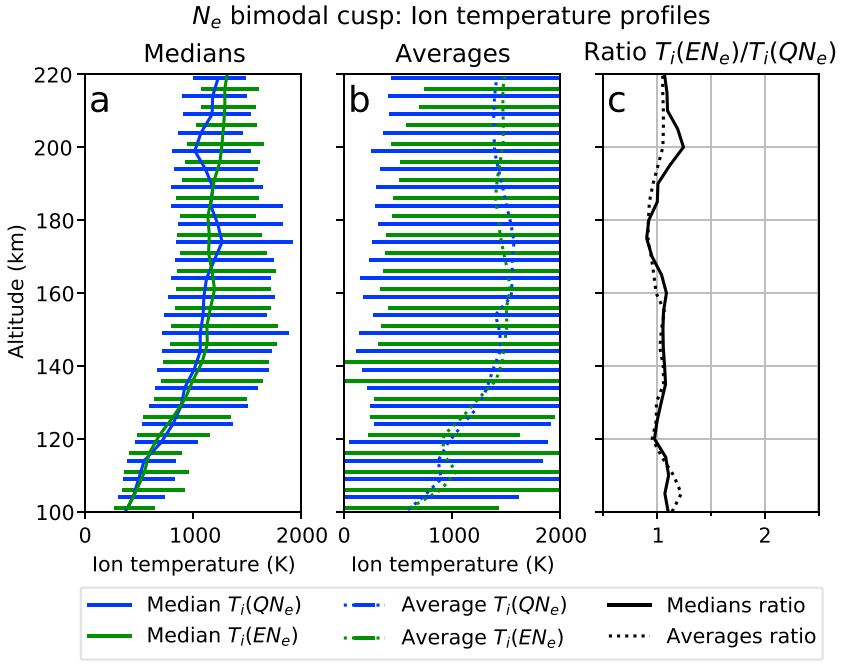

Figure 9. N_e bimodal cusp: Comparison of median and average quiescent and reconnection-enhanced T_i. Error bars as in Figure 8.

Average and standard deviation are well suited to describe data that follow a Gaussian distribution. Our T_i data in particular have a long-tail distribution, as can be seen in Figures 4, 5, and 7. The sensitivity of the average to outliers also enlarges the error bars. The median, with percentile error bars, seems a better description of these data.

Figure 9 tests the usefulness of enhanced N_e as an indicator of enhanced T_i. The question is, does enhanced N_e mean that T_i is also enhanced, and conversely does quiescent N_e mean that T_i is also quiescent? If yes, then the profiles shown for $T_i(\mathrm{QN}_e)$ and $T_i(\mathrm{EN}_e)$ should be significantly different (i.e., one profile should not be within

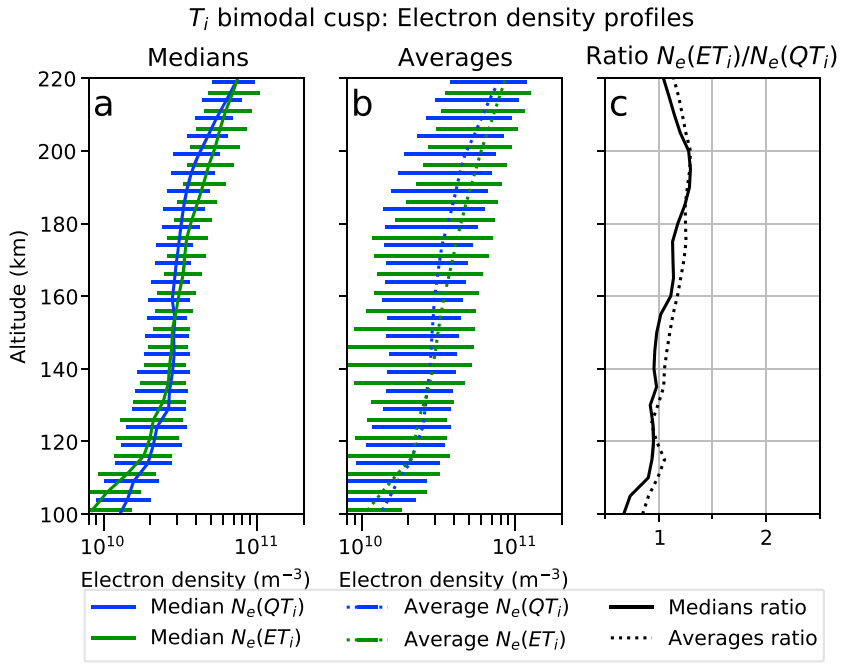

Figure 10. T_i bimodal cusp: Comparison of median and average quiescent and enhanced N_e. Error bars as in Figure 8.

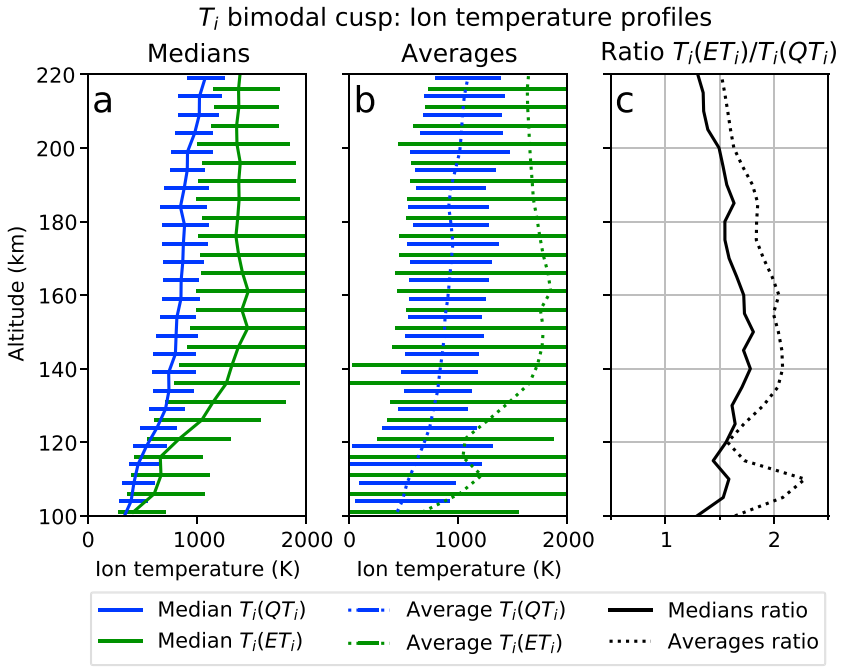

Figure 11. T_i bimodal cusp: Comparison of median and average quiet and active T_i. Error bars as in Figure 8.

the other's error bars). Similarly, Figure 10 tests the usefulness of enhanced T_i as an indicator of enhanced N_e. We find that the presence of enhanced N_e in a volume at 175–200 km does not make it likely that T_i is also enhanced in the same volume. Conversely, we find a small indication for enhanced T_i as an indicator of enhanced N_e, but the error bar overlap is large and this indication is not significant.

We therefore find that dividing the cusp observations into two according to one controlling variable does not provide a good predictor for the other controlling variable: The T_i bimodal profiles $N_e(\mathrm{QT}_i)$ and $N_e(\mathrm{ET}_i)$ show that enhanced T_i is not a useful proxy for enhanced N_e, and similarly the N_e bimodal profiles show that enhanced N_e is not a useful proxy for enhanced T_i, in the field-aligned mode. Several factors contribute to this.

The radar return signal strength is proportional to the electron density. Plasma temperature measurements by ISR depend on fitting a model curve to the radar return spectrum, leading to larger relative errors in the fitted temperature when the electron density is low and the return signal weak. In our data, median σT_i is >300 K for data points where $N_e \sim 10^{10}$ m^{-3} and <100 K for $N_e \sim 10^{11}$ m^{-3}. Weaker return signal is likely to bring the average up, since too low T_i values are more easily identified and filtered out than too high T_i values.

We are assuming that dayside reconnection is the primary source of ionizing precipitation and transient flow shears in the dark cusp. The field-aligned data contains some distinct events which clearly show a strong T_i enhancement accompanying a N_e enhancement, usually ~1 min offset depending on IMF B_Y. However, there are also clear T_i enhancement without a clear N_e enhancement, and vice versa. The small but significant separation in space and time of the enhanced N_e and T_i signatures means that some radar measurements will be quiescent in one signature and enhanced in the other.

Ideally, we would have a situation where the cusp is fully bimodal—either the cusp is fully quiescent or it is fully enhanced. Unfortunately, nature is reluctant to present ideal cases. Reconnection events will vary in strength, and reconnection events take some time to become fully enhanced, and to fade to background again.

Although cusp reconnection is often described as bursty, it is possible that there could be a background "trickle" of electron precipitation from slow continuous energy and plasma transfer at the magnetopause, which would raise the N_e somewhat without affecting T_i much—a plasma flow of ~500 m/s is difficult to detect by T_i observation—while still allowing for larger bursts of energy transfers on top of the semienhanced N_e background. Therefore, the lesson learned here is that simultaneous measurements of N_e and T_i are needed when calculating actual energy deposition rates.

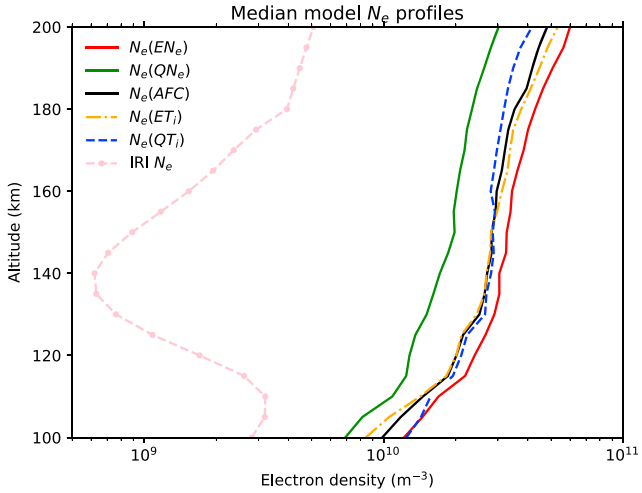

Figure 12. The various statistical cusp N_e profiles.

The amount of quiescent and reconnection-enhanced data each day varies greatly, as shown in Table 1. When the IMF turns north and reconnection stops, we expect quiescent conditions, and the polar cap will frequently contract and pull the cusp poleward out of the radar beam when this happens. For this reason the field-aligned data do not give a complete picture of the cusp, and the ratio of field-aligned measurements listed as "quiescent" and "enhanced" is not a good measure of how frequent reconnection occurs. We need the scanning mode data as well to get good statistics on maximum T_i in the cusp, as the scanning mode is always able to observe a significant portion of the cusp in each scan.

Figure 12 shows the median model N_e profiles calculated above. Also shown for comparison is the median IRI2012 profile for the input data. The empirical profiles at 200 km altitude range from $3\times10^{10}\mathrm{m}^{-3}$ ($N_e(\mathrm{QN}_e)$) to $6\times10^{10}\mathrm{m}^{-3}$ ($N_e(\mathrm{EN}_e)$). Notably, the IRI2012 profile is less than N_e(AFC) by an order of magnitude at 200 km and is a very different shape from the empirical profiles. The IRI model is an empirical model producing monthly averages. The cusp is a relatively small, dynamic, and highly variable structure, and so it gets mixed up with noncusp data when averaging. This confuses the IRI picture of the cusp. Although new data are absorbed into the model with every iteration of IRI, it is not designed to handle the cusp as a special case, nor does it, as a climatological model, reproduce transient enhancements such as these we study here.

3.6. Energy Deposition Rates

Empirical N_e profiles in hand, we can model the electromagnetic (EM) energy deposition rates in the cusp. For this purpose we use the flow shear-driven equation (5) and a range of plausible flow shear velocities. The EM energy deposition rate increases linearly with N_e and quadratically with flow shear. The difference between the median $T_i(\mathrm{ET}_i)$ and MSIS T_n in Figure 7 is 470 K at 200 km altitude, which corresponds to an ion-neutral flow shear of 700–750 m/s depending on neutral composition (see equation (4) and Figure 1). We show deposition rates for selected empirical N_e profiles for the shear velocities 750, 1500, 2000, 3000 m/s (two doublings and an intermediate velocity). The most important energy deposition rates at 200 km altitude are summarized in Table 2.

Table 2. Summary of Dark Cusp Energy Deposition Rates (Units of $\mathrm{W/m}^3$) at 200 km Altitude for Various N_e Profiles and Ion-Neutral Flow Shears

N_e at 200 km ($\times10^{10}\mathrm{m}^{-3}$)		ΔV = 750 m/s ΔT = 470 K[a]	ΔV = 1500 m/s ΔT = 1900 K	ΔV = 2000 m/s ΔT = 3400 K	ΔV = 3000 m/s ΔT = 7700 K
IRI N_e	0.51	3.6×10^{-10}	1.4×10^{-9}	2.6×10^{-9}	5.9×10^{-9}
$N_e(\mathrm{QN}_e)$	3.0	2.1×10^{-9}	8.5×10^{-9}	1.5×10^{-8}	3.5×10^{-8}
$N_e(\mathrm{EN}_e)$	6.0	4.2×10^{-9}	1.7×10^{-8}	3.1×10^{-8}	7.0×10^{-8}
$2\times N_e(\mathrm{EN}_e)$	12	8.4×10^{-9}	3.4×10^{-8}	6.1×10^{-8}	1.4×10^{-7}

[a]Corresponding temperature enhancement at 200 km.

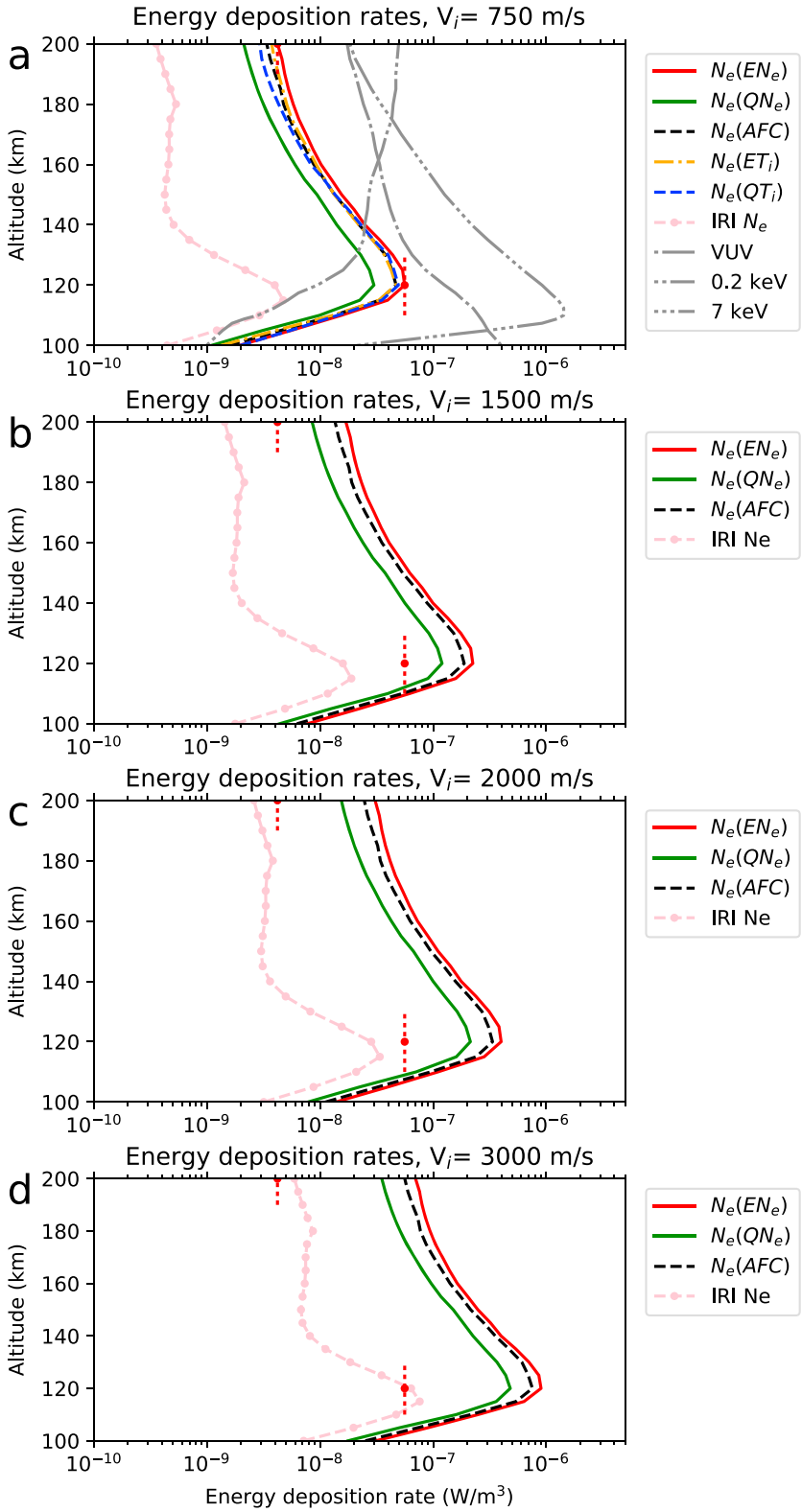

Figure 13. Energy deposition rates of model N_e profiles when ΔV = (a) 750, (b) 1500, (c) 2000, (d) 3000 m/s. (a) also shows particle/vacuum ultraviolet (VUV) profiles from *Thayer and Semeter* [2004]. Dashed red vertical lines mark the value of $N_e(\mathrm{EN}_e)$ for ΔV = 750 m/s, at 120 km (peak) and 200 km (top) altitude. V_i values refer to applied V_i at 200 km. The rapid dropoff below 120 km is due to collisional quenching of V_i.

Table 3. Enhancement in Percent of Energy Deposition Rates for $N_e(EN_e)$ at Peak (130 km) and Topside (200 km) Altitudes for Higher Flow Shears (ΔV Specified at 130 and 200 km[a])

Altitude	$\Delta V_{130} = 704$ m/s $\Delta V_{200} = 750$ m/s	$\Delta V_{130} = 1406$ m/s $\Delta V_{200} = 1500$ m/s	$\Delta V_{130} = 1867$ m/s $\Delta V_{200} = 2000$ m/s	$\Delta V_{130} = 2793$ m/s $\Delta V_{200} = 3000$ m/s
130 km	100%	400%	713%	1605%
200 km	100%	403%	729%	1662%

[a] ΔV is altitude corrected using equations (7) and (8).

Figure 13 shows energy deposition rates calculated for selected N_e profiles shown in Figure 12 for different flow shears, using equation (6) with ΔV modified by equation (8). Also shown for reference (in grey) are the energy deposition rates presented by *Thayer and Semeter* [2004] for solar vacuum ultraviolet (VUV) radiation (dot-dash line), substorm precipitation with 0.2 keV characteristic electron energy (dot-dot-dash), and substorm precipitation with 7 keV characteristic energy (dot-dot-dot-dash). Their deposition rates are calculated for summer conditions at the Søndre Strømfjord site on Greenland, and heating deposition from VUV will be negligible for ESR winter data at these altitudes.

Figures 13b–13d show only the IRI N_e, $N_e(QN_e)$, $N_e(AFC)$, and $N_e(EN_e)$ profiles, to reduce clutter. Figures 13a–13d show energy deposition rates for flow shears of 750 m/s, 1500 m/s, 2000 m/s, and 3000 m/s, respectively. The vertical red marks at 130 and 200 km in all subfigures mark the $N_e(EN_e)$ deposition rate for $\Delta V = 750$ m/s at those altitudes, for comparison between subfigures.

Table 2 lists the various deposition rates at 200 km altitude for the IRI N_e, $N_e(QN_e)$ and $N_e(EN_e)$ profiles. Flow shears are listed with approximate equivalent temperature enhancement (ΔT) at 200 km altitude assuming $T_n = 1000$ K and MSIS composition. By coincidence, $N_e(EN_e)$ is very close to $2 \times N_e(QN_e)$ at the 200 km altitude gate. We have also added the deposition rate for $2 \times N_e(EN_e)$ which has an occurrence rate of ~13%, see Figure 17.

Table 3 shows energy deposition increase for increasing flow shear relative to $\Delta V = 750$ m/s at peak deposition altitude (130 km) and top of the altitude range of interest (200 km).

Figure 13 and Table 2 show that the ΔV flow shear magnitude has the greatest effect on the magnitude of the energy deposition rate, but not so great that the variation in N_e can be ignored. However, as shown earlier, temperature (and hence flow shear) enhancements and N_e enhancements do not correlate well. As the IRI2012 model N_e profile is less than $N_e(EN_e)$ by an order of magnitude, it follows that the deposition rate from the IRI2012 profile is also less by an order of magnitude compared to the deposition rate from $N_e(EN_e)$. A flow shear of more than ~2500 m/s (not shown) is required for the IRI N_e profile to have a deposition rate comparable to $N_e(EN_e)$ at 750 m/s.

3.7. Effect of Neutral Wind

The neutral wind is implicit when using measured T_i enhancements but is important to consider when using V_i for energy deposition calculations, as we have done for Figure 13. A cursory inspection of SCANDI [*Aruliah et al.*, 2010] Fabry-Pérot data quicklooks from 22 January 2012 suggests that the neutral wind at 630.0 nm emission altitudes (assumed 250 km) varies from stagnant to up to 600 m/s near the ESR beam, though only up to around 400 m/s in the time period we have defined as cusp. A significant rotation of the neutral wind can also be seen. SuperDARN [*Ruohoniemi et al.*, 1989; *Greenwald et al.*, 1995] plasma flow quicklooks suggest that the plasma convection was enhanced when neutral wind speeds were enhanced, but neutral wind and plasma drift were not always in the same direction.

Since the direction of the initial flow channel after reconnection is largely controlled by IMF B_Y, the effect of the neutral wind flow on ion heating can be significant. Let us consider a hypothetical case where the neutral wind happens to be 250 m/s along lines of constant MLAT. Between two reconnection events IMF B_Y flips from strongly negative to strongly positive, so that the reconnection-driven flow is first antiparallel to V_n and then parallel to it. In both events the V_i magnitude is 1750 m/s in the ground frame. As shown in Figure 1 and Table 2, a ΔV=2000 m/s at 200 km corresponds to a $\Delta T = 3400$ K, while $\Delta V = 1500$ m/s corresponds to $\Delta T = 1900$ K, a difference of 1500 K. From either of equation (5) or (6), this flow reversal leads to a halving of the energy deposition, without changing the magnitude of either V_i or V_n.

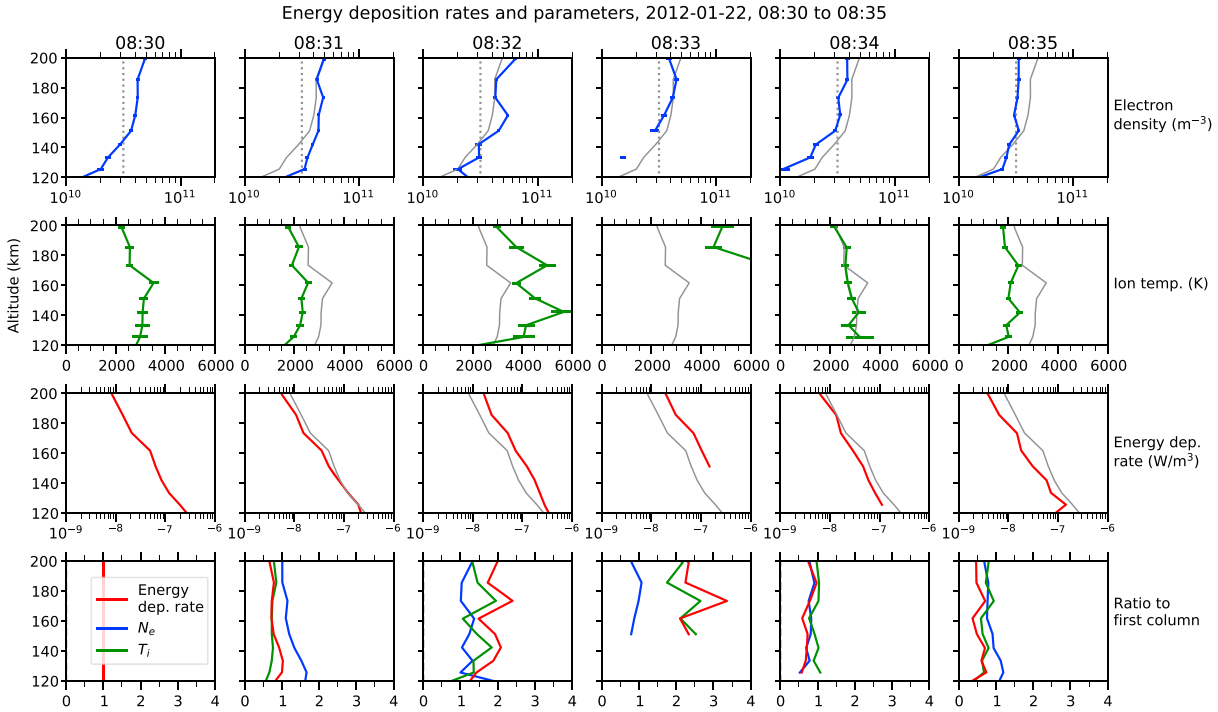

Figure 14. A sequence of radar measurements showing the rapid variation in energy deposition rate as an event passes through the radar field of view.

3.8. Case Study

We proceed now to a case study. Figure 14 shows a short sequence of field-aligned radar measurements from 22 January 2012. This sequence is representative of an active day with many consecutive reconnection events. Figure 14 (first row) shows electron density, Figure 14 (second row) shows ion temperatures, and Figure 14 (third row) the energy deposition rate, calculated using equation (5). The grey line in each column after the first is the measurement shown in the first column of the row. Figure 14 (fourth row) shows the ratio of the N_e, T_i and energy deposition rate relative to the first column, i.e., value of the parameter in the current column divided by the same parameter in the first column.

Figure 14 (first row) has $N_e = 10^{10.5} = 3.2 \times 10^{10}$ m^{-3} marked by a dotted vertical line. This is the threshold we have used for N_e bimodal cusp to indicate enhanced ionization in the dark cusp. N_e is already high in Figure 14 (first column) because this example is taken from a close-packed sequence of events on top of an already enhanced "quasi-background," and N_e was elevated to a greater or lesser extent throughout.

The figures show rapid variation in both N_e and T_i from minute to minute, and corresponding rapid variation in energy deposition rate. The maximum for this sequence occurs at 08:33, with the minimum at 08:35. At 200 km altitude the maximum deposition rate is 2×10^{-8} W/m^{-3}, and the minimum is 4×10^{-9} W/m^{-3}, a factor of 5 difference in 2 min. The largest variation in deposition rate comes from the variation in T_i, but the contribution from variation in N_e should not be ignored.

Lühr et al. [2004] observed intense, fine-structured (kilometer-scale) Birkeland currents in the cusp whenever a neutral density enhancement was observed. *Watermann et al.* [2009] and *Lühr and Marker* [2013] tied these currents to magnetopause reconnection, possibly with turbulent breakup of current sheets. Fine-structured currents will set up fine-structured horizontal plasma flow and ion frictional heating, which when convecting across the ESR beam will be seen as rapid variation in T_i, and in energy deposition rates.

4. Maximum T_i Occurrence Rates

4.1. From ESR Scanning Mode Data

The strength of the scanning mode is the ability to cover a large area quickly. We used this method to gather data on the occurrence rate of heating events on open field lines near the cusp. We selected 6 days from

Table 4. Overview of ESR Scanning Mode Data Used and *Kp* Values

Date	Number of Scans	*Kp* Index 06–09 UT	*Kp* Index 09–12 UT
15 December 2001	100	2	2+
16 December 2001	91	3+	2+
17 December 2001	103	3	3
18 December 2001	85	2	2+
19 December 2001	112	2	3–
20 December 2001	103	1	1+
Total	594		

December 2001 which had data from both sides of magnetic noon and no long interruptions, and good cusp signatures. Table 4 shows an overview of the amount of scanning data used.

The scanning mode data of the ESR were analyzed for signatures of T_i heating events. Since the data have large statistical error bars due to the short integration time, we looked for T_i structures extended along lines of constant magnetic latitude for the azimuth scanning mode, and structures extended along the geomagnetic field for the elevation scan mode. When we found such a structure, we assigned to it the highest T_i value observed within the structure (while taking data noise into account). When no clear structure was found, we assigned an average background value for T_i.

We would expect these T_i structures to be accompanied by a nearby enhancement in N_e around 175–200 km altitude. However, the scanning mode field of view is much smaller at low altitude than at high altitude, frequently missing the area where such an enhancement would be found. In addition, the coarse altitude resolution of the scanning mode is not well suited to identifying such enhancements. Where we could see such N_e enhancements, we took them into account when compiling statistics.

We looked at scanning data mainly from ~200 to 400 km altitude. Regions of the scans not on open field lines, as indicated by low T_e, were excluded. Due to the large error bars in the data, we noted temperatures in increments of 500 K. No temperature lower than 1000 K was registered. One maximum temperature was noted for each scan, even if multiple events were observed in a single scan.

At 30° elevation, 400 km altitude corresponds to 740 km range, and data beyond this range generally had too poor signal-to-noise ratio (SNR) to be useful in the scanning modes because of the very short integration time. The altitude resolution of the scanning modes is poor below 200 km, each altitude bin spanning several scale heights. The scanned area at 150–200 km altitude is small relative to the higher *F* region data, and events poleward or equatorward of the radar may not enter this low-altitude region of the radar scan at all. At higher elevations, the low electron density at high altitude also limits the strength of the return signal.

Figures 15 and 16 show examples of the scanning data. Figure 15 shows a scan in elevation. The diagonal gray lines show AACGM MLAT and the inclination of the geomagnetic field, and the arrow below the data shows direction of radar scanning motion. The heating event around 77.5° MLAT (ringed in black) is judged to be around 4500 K peak temperature based on the data below 400 km altitude. The other heating event (ringed in gray) between 74 and 75° MLAT is lower and hence not included in the statistics. As mentioned, we only count one event per scan.

Figure 16 shows a scan in azimuth, with a constant elevation of 30°. The black circle segments in Figure 16 show 150, 200, 400, and 600 km altitude, corresponding to 290, 380, 740, and 1075 km line-of-sight ranges. The black arrows show the direction of radar scanning motion. The red lines show AACGM MLAT. AACGM coordinates are altitude-dependent since they follow the geomagnetic field lines (cf. Figure 15). To make it easier to study the radar data relative to geomagnetic latitudes in Figure 16, the coordinates of the radar data and the altitude lines have been projected along the geomagnetic (IGRF) field to 250 km altitude, and the lines of AACGM MLAT are drawn for the same altitude.

The strongest heating event is seen at 74° MLAT in Figure 16c, ringed in black. The heating event is observed to be aligned to lines of MLON, located in the middle of a strong flow channel seen in Figure 16d. Allowing for error bars, we judge the event to be at approximately 4000 K peak temperature. There are strong heating

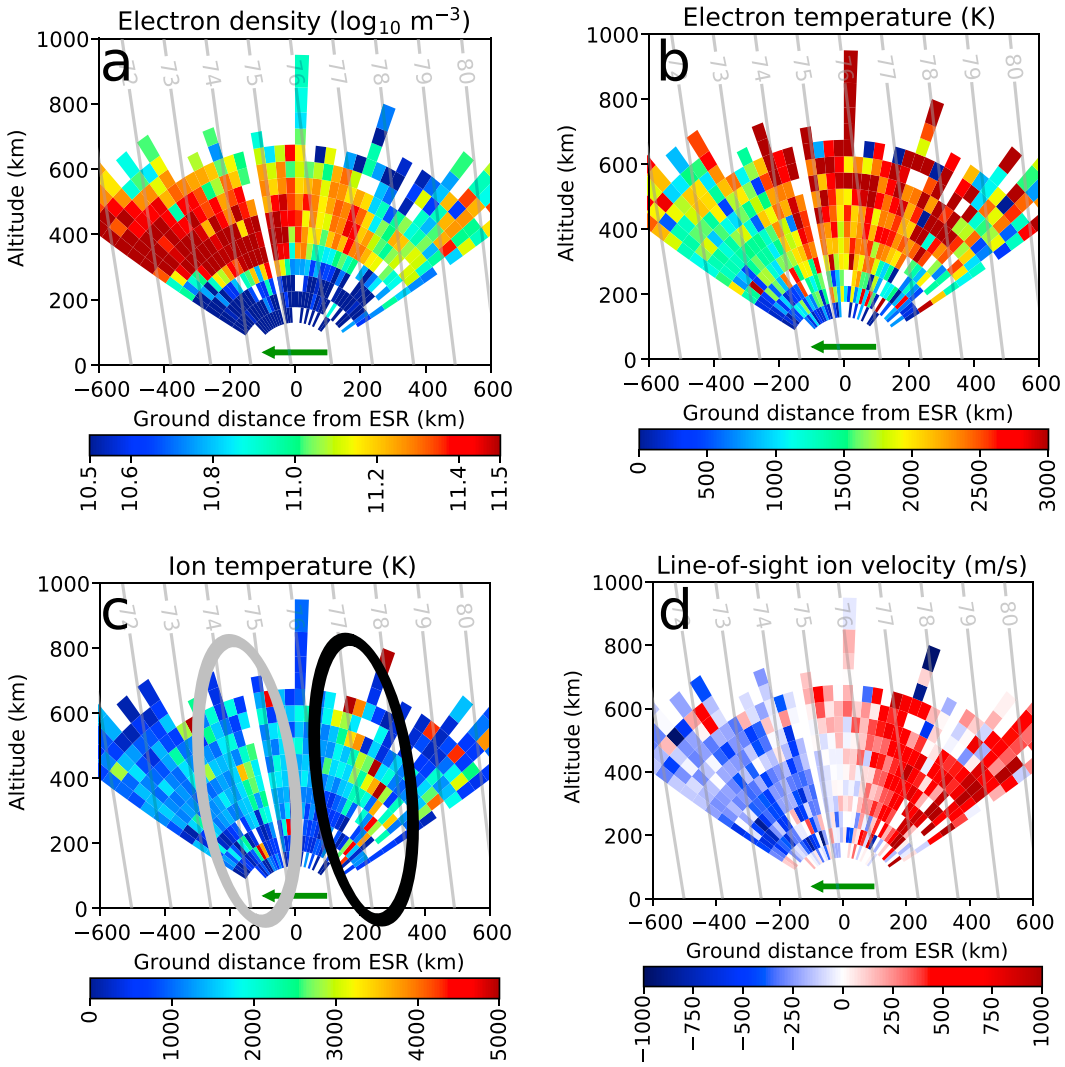

Figure 15. A scan in elevation from 18 December 2001, from 08:25 to 08:27 UT. Grey lines indicate geomagnetic latitude (MLAT). An ion heating event rated at 4500 K is located at 77–78° MLAT. The smaller event between 74 and 75° MLAT is not included in the statistic. The arrow below the fan shows the direction of radar scanning motion.

regions also further north, also associated with strong flows but not counted in our statistics since we count the strongest event per sweep.

Selecting the peak temperature from a heating event in low SNR data is not easily automatable. To find the heating events in the scanning data, we studied multiple plots of each scan, looking for regions of structured heating. For the azimuth scanning mode, this meant that the heating structure must be elongated and extended in MLON. Heating events should be colocated with channels of increased ΔV. We then assessed the temperatures along this flow channel, estimating its maximum value. To correct for low SNR, we required that several range gates along the structure had roughly the same temperature and excluding the very highest values as outliers.

We cannot easily see flow channels directly in elevation scans, nor the east-west extent of the heating. Instead, we require that the heating be in a structure that is aligned with the geomagnetic field and extends throughout the *F* region or as much of it as is within the effective field of view. The same procedure as above was applied to find the maximum temperature of the event.

In a few cases we looked at preceeding and following scans to check if faint structures were real or noise and excluded/included them accordingly in the statistics. Other than this, each scan was evaluated individually and independently when searching for temperature maxima.

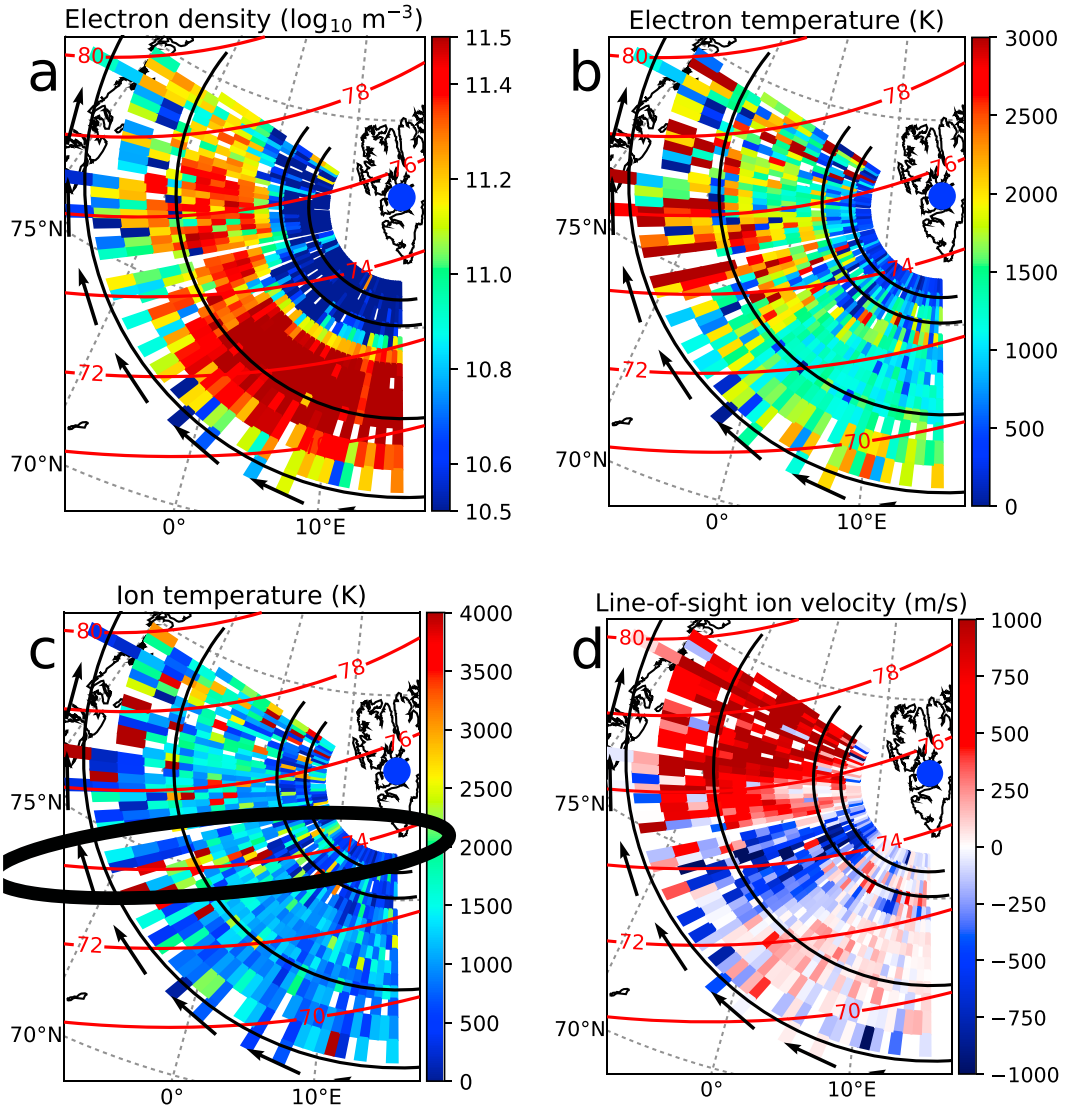

Figure 16. A scan in azimuth from 19 December 2001, from 08:41 to 08:44 UT. Red lines indicate geomagnetic latitude (MLAT). An ion heating event rated at 4000 K is located at 74–75° MLAT. Blue dot marks ground location of ESR. Black lines mark distance from radar (150, 200, 400, 600 km). Black arrows near 600 km line show the direction of radar scanning motion. MLAT lines and radar fan are projected along the magnetic field to 250 km altitude.

Figure 17 shows cumulative histograms of T_i, for (a) both scanning modes (combined, 594 scans) and (b) the field-aligned cusp data (558 measurements). Figure 17a (scanning mode) uses per scan maximum T_i, while Figure 17b shows maximum T_i for each integration period in the altitude range 175–200 km, 150–175 km, and 130–150 km. The field-aligned data are discussed further in section 3.

The height of each bar shows the occurrence rate for that temperature or higher; i.e., the maximum observed T_i in the scanning mode (Figure 17a) was ≥1000 K 100% of the time, ≥2000 K 88% of the time, etc. The variation in occurrence rates from day to day was small for the scanning modes.

4.2. Comparison to Field-Aligned Data

Comparing Figures 17a and 17b, we see that the scanning mode data sees enhanced temperatures much more frequently than the field-aligned cusp mode. The difference is probably due to the very different fields of view, and the difference in integration time. The azimuth scanning mode searches a large field of view for heating events, while the field-aligned mode is static and has a small field of view which events convect across rapidly. Enhanced T_i may vary along the flow channel so that the static radar beam may not encounter the maximum temperature of the channel, while the azimuth scanning mode can see a large portion of the

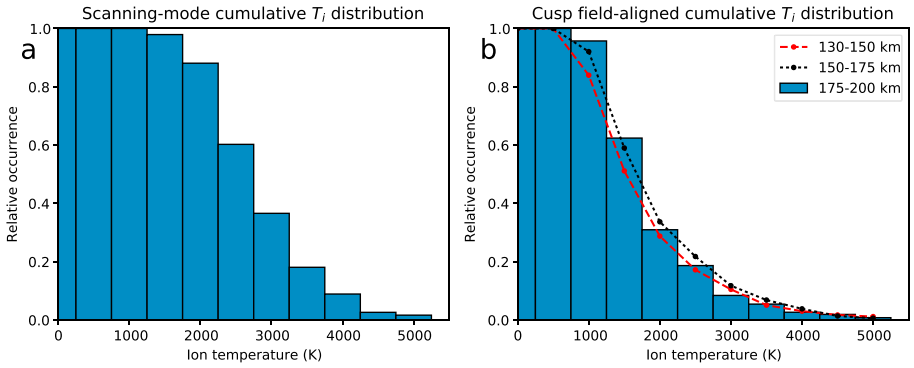

Figure 17. Cumulative histograms of relative frequency for an ion temperature observed to exceed the indicated T_i for (a) scanning mode data and (b) field-aligned cusp data. In the scanning mode this refers to the highest T_i seen within the field of view of each scan and in the cusp. For field-aligned data the T_i value for each measurement is the maximum T_i between 175–200 km altitude. The difference in occurrence rates is largely due to the different fields of view, with the field-aligned field of view being less likely to encounter a heating event.

flow channel every 3–5 min. The elevation scanning mode, like the field-aligned mode, will only see cross sections of heating events but can see them in the upper *F* region up to ~400 km equatorward or poleward of the radar.

In addition, the 60 s integration time of the static beam may smooth out extrema it encounters, as they are likely to convect past fairly rapidly.

Since there is some variation of T_i with altitude, Figures 17a and 17b do not show quite the same thing. The "background" temperature is higher in Figure 17a since quiescent T_i is somewhat higher at high altitudes than at 175–200 km (~1200–1500 K versus ~800–1000 K). Conversely, the enhanced T_i will be lower at higher altitude than at lower altitude in the same flux tube, see Figure 1 (e.g., a $\Delta V = 2000$ m/s gives a temperature enhancement ΔT_i=3850 K at 150 km altitude, but ΔT_i=2590 K at 350 km). Since Figure 17a uses mostly upper *F* region data, it probably somewhat overestimates the occurrence of ~1500 K T_i and underestimates the occurrence of highly enhanced T_i, relative to what we would find if we could measure T_i at 175–200 km over the entire area covered by the scanning modes.

Figure 18 shows four histograms of the per-measurement maximum T_i distribution for field-aligned data. Figures 18a and 18b show T_i data for the times when the radar beam is within the cusp, i.e., the AFC data set. Figures 18c and 18d show data for those times between 07 and 11 UT each day when the radar beam is *not* in the cusp. Figures 18a and 18c show occurrence rate histograms of T_i, and Figures 18b and 18d show cumulative occurrence rate histograms of the same data.

All subfigures show maximum T_i measured between 175 and 200 km altitude for each radar measurement, shown as bar graphs. In addition, T_i histograms for the altitude ranges 130–150 km and 150–175 km are shown as line graphs. The histograms in Figures 18a and 18c are normalized so that the sum of the bar heights (point heights) is 1 for each altitude range, and the height of each bar is equal to the fraction of the total number of measurements represented by that bar. The cumulative histograms in Figures 18b and 18d are normalized so that the height of the first bar (point) is 1.

We have focused mainly on 175–200 km altitude in this paper, since theoretical work [*Carlson et al.*, 2012] shows that this altitude range is where heating will have a major impact on upwelling. The other ranges are not expected to have any significant effect on neutral upwelling on the timescale of a reconnection-driven heating event (~15 min) [*Carlson*, 1998, 2007; *Carlson et al.*, 2012]. However, it is worth checking if the lower altitudes show the same heating distribution as 175–200 km. The histograms for the altitude ranges shown in Figure 18a are quite similar to each other, although T_i tends toward somewhat lower values at lower altitudes, consistent with lower T_n at lower altitudes. The similar shape of the curves suggests that T_i measured below 175 km altitude can be used to infer heating between 175 and 200 km altitude, useful for example for in situ measurements such as sounding rockets used to probe cusp events.

Comparing the noncusp data in Figure 18c, we see that enhanced temperatures are less common at all altitudes outside the cusp.

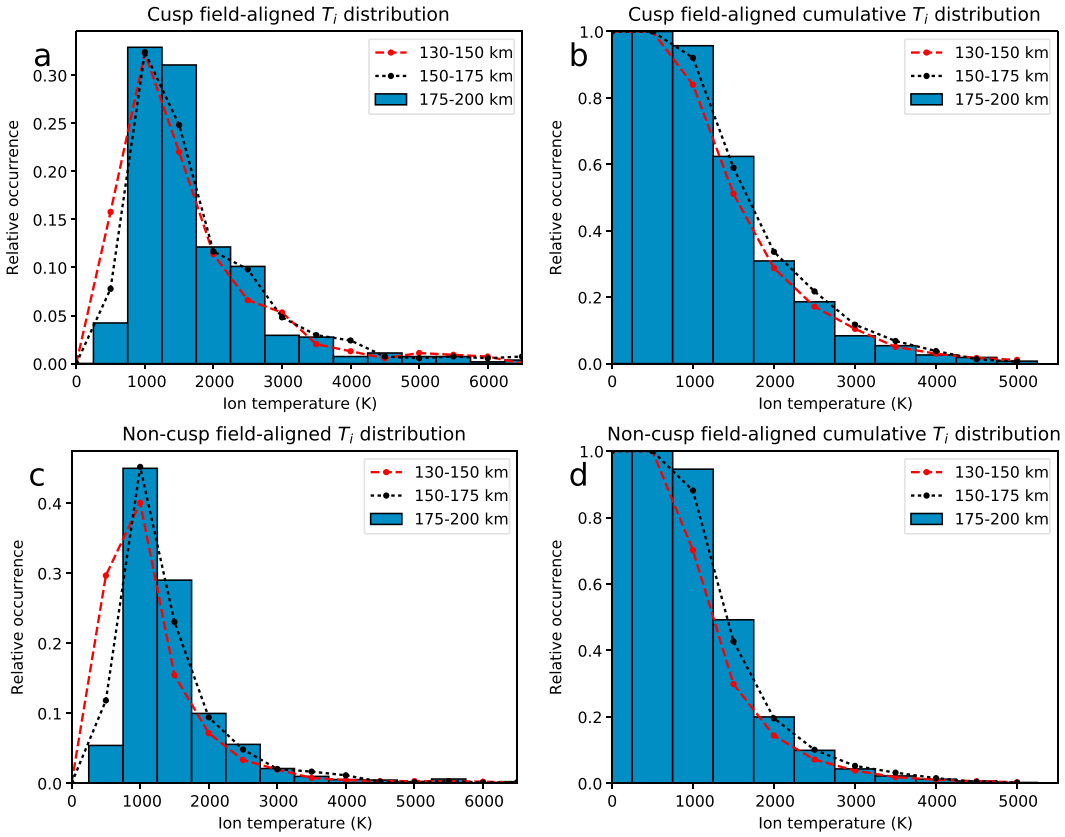

Figure 18. Histograms of observed field-aligned per-measurement maximum ion temperatures. (a and c) Occurrence histograms; (b and d) cumulative occurrence histograms. Figures 18a and 18b show field-aligned data from the cusp; Figures 18c and 18d show field-aligned data from outside the cusp between 07–11 UT, in three different altitude ranges. Temperature enhancements are seen to be more common in the cusp than outside the cusp, and the similar shape of all the altitude range histograms indicates that the temperature enhancements occur in all three altitude ranges, consistent with ion frictional heating.

Figures 18b and 18d shows again that the noncusp ionosphere is somewhat colder than the cusp ionosphere in the altitude ranges examined: cusp $T_i \geq 1500$ K in 175–200 km around 60% of the time versus ~50% outside the cusp, and at the lowest altitude range $T_i \geq 1000$ K occurs ~85% of the time in the cusp versus ~70% outside the cusp. The larger enhancements are also somewhat less common outside the cusp than within. Using the observed ion temperatures as a proxy for ongoing reconnection events, the field-aligned data predict fewer strong events than the scanning mode, which has a much larger field of view.

To summarize, we observe in the scanning mode data that an occurrence of T_i of 3000 K or greater can be expected some 35% of the time somewhere in the cusp, and that an occurrence of at least 2000 K T_i is very common. $T_i \geq 3500$ K, likely to cause neutral upwelling, is observed around 18% of the time. These values can be used as proxies for the likelihood that a reconnection event of a certain magnitude is ongoing at any given moment. The same T_i occurrence distribution is not observed for field-aligned data, which is probably due to a combination of experiment geometry and smoothing due to long integration.

5. Summary and Conclusions

Lühr et al. [2004] drew the attention of the scientific community by developing and flying a dramatically improved accelerometer, measuring previously unobservable density/drag enhancements near 400 km over the cusp. The magnitude of the enhancements exceeded 20% half the time including up to doublings. A large number of papers have since sought to explain and model these enhancements. Accomplishing this remains a challenge. All models require as input, values of plasma flow speed, and also of electron density below 200 km [$N_e(h < 200$ km)] or equivalently conductivity profiles or precipitating particle spectra.

Table 5. Theoretical Expectations: Using N_e and T_i Thresholds to Find Enhanced N_e and T_i

	Reconnection-Enhanced T_i	Reconnection-Enhanced N_e
Use T_i data to find	Yes	No
Use N_e data to find	Poorly	Yes

Our premise here is the need for an improved model for the electron density below 200 km and for the range of plasma flow speeds experienced over the cusp. This need is well recognized by the community.

Carlson [1998] had previously shown theoretically that the cusp thermosphere should respond to variable overhead energy deposition with far greater sensitivity than the rest of the auroral oval. He based his conclusion on the nonlinear response of the thermosphere to known ionospheric variability in plasma flow speeds [V_i], plus linear dependence on bottomside ionosphere [N_e] electron density/conductivity. Quoting the *Lühr et al.* [2004] quantitative observational facts, it was shown that known variability in V_i and $N_e(h < 200$ km) both could [*Carlson*, 2007] and in fact did [*Carlson et al.*, 2012] quantitatively account for the up to twofold drag prediction errors. The latter paper showed significant improvement by use of data-based (observed) empirical values for $N_e(h < 200$ km) and observed V_i variability ~0.5–3 km/s rather than commonly used static average values, and urged doing so. Publications citing this work quickly confirmed the significant improvement promised [*Wilder et al.*, 2012; *Zhang et al.*, 2012; *Deng et al.*, 2013]. However, there has been no consistent use of an improved $N_e(h)$ model, and no use of realistic versus average plasma flow values.

We have searched a 3 year ESR database and used 594 scans across the cusp, plus 558 field-aligned measurements around the cusp, to find observationally based empirical estimates of sorely needed $N_e(h)$ and V_i flow fields. We find use of these data-based values instead of commonly used averaged models (averages smooth out flow jet spikes in a nonlinear thermosphere-ionosphere system), increases energy deposition rates (relative to average models) by up to a factor of 30 for realistic plasma flow V_i, and a factor of ~10 for N_e in the dark cusp.

We have calculated profiles of electron density and ion temperatures typical of the dark winter cusp and shown the associated rate of EM energy deposition into the thermosphere. Reconnection-enhanced N_e at 175–200 km altitude is around double that of quiescent N_e and is consistently an order of magnitude greater than that predicted by the IRI2012 model. We have also mapped occurrence rates of ion temperature enhancements in or near the cusp.

We have calculated the following: (1) the frequency of occurrence of magnetic reconnection events in or near the cusp, as identified by occurrence rate of T_i maximum temperatures in the scanning modes; (2) the magnitude of the flow shear in these reconnection flow jets, as identified by the distribution of temperature enhancements and median field-aligned profiles of $T_i(ET_i)$; (3) the typical N_e enhancement at 175-200 km altitude at the foot point of newly opened flux tubes.

Ion temperatures exceeding 3000 K are common in or near the cusp, occurring around 35% of the time. The space and time evolution of N_e and T_i enhancements are different, so the presence of enhanced N_e in a radar volume does not imply presence of enhanced T_i in the same volume, and vice versa.

The IRI model is significantly underestimating the plasma densities in the lower *F* region and hence is not useful as model input for satellite drag due to upwelling from lower altitudes. In the altitude region 175–200 km for quiet cusp conditions the magnitude of the IRI model profile is only ~17% of the measured median cusp values obtained by ESR, and for active cusp conditions the IRI N_e profile only is ~9% of the measured profile, a full order of magnitude in difference (cf. Figure 12). Similarly for modeled, the model T_i values represents an underestimate of ~65% for reconnection-enhanced T_i, while it accurately reproduces quiescent T_i (95–105%) in the altitude range 175–200 km.

It should be noted that these parameters are rapidly fluctuating in the cusp, and as demonstrated in a case study may vary by a factor of 5 in 2 min (cf. Figure 14).

Prior work [e.g., *Lockwood and Carlson*, 1992; *Carlson et al.*, 2004, 2006] leads us to know that reconnection-enhanced N_e precedes in time the reconnection-induced flow jet, which cumulatively produces the T_i enhancement through frictional drag heating. The relative time delays and durations expected are quantitatively defined and documented in the observations given in the latter two of these references. For this reason

Table 6. Empirical Findings

	Reconnection-Enhanced T_i	Reconnection-Enhanced N_e
Use T_i data to find	Yes [1.6–2x]	No [1.2x, large σ]
Use N_e data to find	No [0.9x, large σ]	Yes [2–2.3x]

we use the N_e data and onset duration of the N_e enhancements to define the activated N_e measurements; we do likewise with the T_i data to identify the activated T_i events. Their separation in time and space and different lifetimes means that one is not a good proxy for the other. Table 5 summarizes these theoretical expectations, and Table 6 shows the empirical findings that confirm our expectations.

The absence of an E layer, seen as an increase in N_e around 90–120 km, but presence of good (precipitation induced) ($\gg 10^9$ m^{-3}) N_e at 150–250 km (while the altitude range 175–200 km is most relevant to heating deposition for upwelling) is used to identify the cusp location. Those events for which we had good optical data (in both red 630.0 nm and green 557.7 nm) confirmed use of this criterion, consistent with a large body of literature.

The results we have presented here will be important to guide model work to use observational data for N_e and T_i rather than using unrealistic model representatives. Since the IRI and the MSIS models do not represent the dynamic cusp, they are useless as input values in energy deposition studies. This study underlines the need for systematic ISR data acquisition in the auroral oval with year-continuous operations over at least one solar cycle to establish parametrized statistical profiles for N_e and T_i. N_e and T_i variability unfortunately do not correlate within a static observation volume. To get the full history of an event, it is necessary to measure the N_e and T_i simultaneously. While this can to some extent be accomplished by a low-elevation radar beam mode, modern volumetric ISR will get a much more complete picture of such events. The phased array 3-D mapping capabilities will be a must for complete understanding of the energy deposition in the cusp.

Acknowledgments
EISCAT is an international association supported by research organizations in Norway (NFR), Sweden (VR), Finland (SA), Japan (NIPR and STEL), China (CRIRP), the United Kingdom (STFC), Germany (DFG, till 2011), and France (CNRS, till 2005). The EISCAT data used in this publication are freely available at http://www.eiscat.se/madrigal/. The SCANDI quicklooks referenced in section 3.7 is available at http://www.ucl.ac.uk/star/research/planets/terrestrial/observation. SuperDARN plots can be found at http://vt.superdarn.org/. Data files containing the profiles in Figure 12 are available at https://zenodo.org/record/556604. The figures in this publication were made with Matplotlib [*Hunter*, 2007]. Thanks to the Norwegian Polar Institute for hosting the University of Oslo's optical instrumentation at Ny-Ålesund, Svalbard. The ground optical data used in this paper can be provided on request to Bjørn Lybekk (bjorn.lybekk@fys.uio.no), who is in charge of the optical database at the University of Oslo. The optical data from the MSP at the Auroral Station/Kjell Henriksen Observatory in Longyearbyen, Svalbard, are available from the observatory website at http://kho.unis.no. This project has been sponsored by the Norges Forskningsråd (Research Council of Norway) grants 230935 and 230996 and partially by National Science Foundation grant AGS-1011921 (H.C.C.). This research is a part of the 4DSpace initiative at the University of Oslo.

References

Aruliah, A., A. Ronksley, D. Johnson, and H. Carlson (2015), *Multi-Instrument and Modelling Study of Small-Scale Upwelling and Density Changes in the Auroral Thermosphere-Ionosphere Region*, vol. 17, EGU2015-13447, Vienna, Austria.

Aruliah, A. L., E. M. Griffin, H.-C. I. Yiu, I. McWhirter, and A. Charalambous (2010), SCANDI — An all-sky Doppler imager for studies of thermospheric spatial structure, *Ann. Geophys.*, *28*(2), 549–567, doi:10.5194/angeo-28-549-2010.

Bilitza, D., D. Altadill, Y. Zhang, C. Mertens, V. Truhlik, P. Richards, L.-A. McKinnell, and B. Reinisch (2014), The International Reference Ionosphere 2012 — An model of international collaboration, *J. Space Weather Space Clim.*, *4*, A07, doi:10.1051/swsc/2014004.

Burns, A. G., T. L. Killeen, and R. G. Roble (1989), Processes responsible for the compositional structure of the thermosphere, *J. Geophys. Res.*, *94*(A4), 3670–3686, doi:10.1029/JA094iA04p03670.

Carlson, H. C. (1998), Response of the polar cap ionosphere to changes in (solar wind) IMF, in *Polar Cap Boundary Phenomena*, edited by J. Moen, A. Egeland, and M. Lockwood, pp. 255–270, Kluwer Acad. Publ., Boston.

Carlson, H. C. (2007), Role of neutral atmospheric dynamics in cusp density and ionospheric patch formation, *Geophys. Res. Lett.*, *34*, L13101, doi:10.1029/2007GL029316.

Carlson, H. C. (2012), Sharpening our thinking about polar cap ionospheric patch morphology, research, and mitigation techniques, *Radio Sci.*, *47*, RS0L21, doi:10.1029/2011RS004946.

Carlson, H. C., K. Oksavik, J. Moen, A. P. van Eyken, and P. Guio (2002), ESR mapping of polar-cap patches in the dark cusp, *Geophys. Res. Lett.*, *29*(10), 1386, doi:10.1029/2001GL014087.

Carlson, H. C., K. Oksavik, J. Moen, and T. Pedersen (2004), Ionospheric patch formation: Direct measurements of the origin of a polar cap patch, *Geophys. Res. Lett.*, *31*, L08806, doi:10.1029/2003GL018166.

Carlson, H. C., J. Moen, K. Oksavik, C. P. Nielsen, I. W. McCrea, T. R. Pedersen, and P. Gallop (2006), Direct observations of injection events of subauroral plasma into the polar cap, *Geophys. Res. Lett.*, *33*, L05103, doi:10.1029/2005GL025230.

Carlson, H. C., T. Spain, A. Aruliah, Å. Skjæveland, and J. Moen (2012), First-principles physics of cusp/polar cap thermospheric disturbances, *Geophys. Res. Lett.*, *39*, L19103, doi:10.1029/2012GL053034.

Carlson, H. C., A. Aruliah, J. Moen, L. Clausen, and Å. S. Skjæveland (2015), *Cause and Effect Linkages: Solar Wind Transient energy input- Polar Thermosphere Response 26th IUGG General Assembly, IAGA Symposium Session ID #26 invited*, Springer, Paris.

Clemmons, J. H., J. H. Hecht, D. R. Salem, and D. J. Strickland (2008), Thermospheric density in the Earth's magnetic cusp as observed by the Streak mission, *Geophys. Res. Lett.*, *35*, L24103, doi:10.1029/2008GL035972.

Cowley, S. W. H., and M. Lockwood (1992), Excitation and decay of solar wind-driven flows in the magnetosphere-ionosphere system, *Ann. Geophys.*, *10*, 103–115.

Cowley, S. W. H., M. P. Freeman, M. Lockwood, and M. F. Smith (1991), The ionospheric signature of flux transfer events, in *Cluster Dayside Polar Cusp*, vol. 330, pp. 105–112, ESA SP, European Space Agency, Nordwijk, Netherlands.

Crowley, G., A. Reynolds, J. P. Thayer, J. Lei, L. J. Paxton, A. B. Christensen, Y. Zhang, R. R. Meier, and D. J. Strickland (2008), Periodic modulations in thermospheric composition by solar wind high speed streams, *Geophys. Res. Lett.*, *35*, L21106, doi:10.1029/2008GL035745.

Crowley, G., D. J. Knipp, K. A. Drake, J. Lei, E. Sutton, and H. Lühr (2010), Thermospheric density enhancements in the dayside cusp region during strong B_y conditions, *Geophys. Res. Lett.*, *37*, L07110, doi:10.1029/2009GL042143.

Demars, H., and R. Schunk (2007), Thermospheric response to ion heating in the dayside cusp, *J. Atmos. Sol. Terr. Phys*, *69*(6), 649–660, doi:10.1016/j.jastp.2006.11.002.

Deng, Y., T. J. Fuller-Rowell, A. J. Ridley, D. Knipp, and R. E. Lopez (2013), Theoretical study: Influence of different energy sources on the cusp neutral density enhancement, *J. Geophys. Res. Space Physics*, *118*, 2340–2349, doi:10.1002/jgra.50197.

Fasel, G. (1995), Dayside poleward-moving auroral forms: A statistical study, *J. Geophys. Res.*, *100*, 11,891–11,905, doi:10.1029/95JA00854.

Greenwald, R. A., et al. (1995), DARN/SuperDARN: A global view of the dynamics of high-latitude convection, *Space Sci. Rev.*, *71*(1–4), 761–796, doi:10.1007/BF00751350.

Grydeland, T., A. Strømme, T. van Eyken, and C. La Hoz (2004), The capabilities of the EISCAT Svalbard radar for inter-hemispheric coordinated studies, *Chin. J. Polar Sci.*, *13*(1), 55–66.

Hedin, A. E. (1991), Extension of the MSIS thermosphere model into the middle and lower atmosphere, *J. Geophys. Res.*, *96*(A2), 1159–1172, doi:10.1029/90JA02125.

Hunter, J. D. (2007), Matplotlib: A 2D graphics environment, *Comput. Sci. Eng.*, *9*(3), 90–95, doi:10.1109/MCSE.2007.55.

Kamiyama, H. (1967), The electron density distribution in the lower ionosphere produced through impact ionization by precipitating electrons and through photoionization by the associated bremsstrahlung X-rays, *J. Geomagn. Geoelectr.*, *19*(1), 27–47, doi:10.5636/jgg.19.27.

Kervalishvili, G. N., and H. Lühr (2013), The relationship of thermospheric density anomaly with electron temperature, small-scale FAC, and ion up-flow in the cusp region, as observed by CHAMP and DMSP satellites, *Ann. Geophys.*, *31*(3), 541–554, doi:10.5194/angeo-31-541-2013.

Liu, H., H. Lühr, V. Henize, and W. Köhler (2005), Global distribution of the thermospheric total mass density derived from CHAMP, *J. Geophys. Res.*, *110*, A04301, doi:10.1029/2004JA010741.

Lockwood, M., and H. C. Carlson (1992), Production of polar cap electron density patches by transient magnetopause reconnection, *Geophys. Res. Lett.*, *19*(17), 1731–1734, doi:10.1029/92GL01993.

Lockwood, M., and S. W. H. Cowley (1988), Observations at the magnetopause and in the auroral ionosphere of momentum transfer from the solar wind, *Adv. Space Res.*, *8*(9), 281–299, doi:10.1016/0273-1177(88)90142-1.

Lockwood, M., J. Moen, S. W. H. Cowley, A. D. Farmer, U. P. Løvhaug, H. Lühr, and V. N. Davda (1993), Variability of dayside convection and motions of the cusp/cleft aurora, *Geophys. Res. Lett.*, *20*(11), 1011–1014.

Lorentzen, D. A., and J. Moen (2000), Auroral proton and electron signatures in the dayside aurora, *J. Geophys. Res.*, *105*, 12,733–12,745.

Lühr, H., and S. Marker (2013), High-latitude thermospheric density and wind dependence on solar and magnetic activity, in *Climate and Weather of the Sun-Earth System (CAWSES)*, pp. 189–205, Springer Atmospheric Sciences, Dordrecht, Netherlands, doi:10.1007/978-94-007-4348-9_11.

Lühr, H., M. Rother, W. Köhler, P. Ritter, and L. Grunwaldt (2004), Thermospheric up-welling in the cusp region: Evidence from CHAMP observations, *Geophys. Res. Lett.*, *31*(6), L06805, doi:10.1029/2003GL019314.

Moen, J., M. Lockwood, P. E. Sandholt, U. P. Løvhaug, W. F. Denig, A. Egeland, and A. P. van Eyken (1996), Variability of dayside high latitude convection associated with a sequence of auroral transients, *J. Atmos. Terr. Phys.*, *58*, 85–95, doi:10.1016/0021-9169(95)00021-6.

Moen, J., D. A. Lorentzen, and F. Sigernes (1998), Dayside moving auroral forms and bursty proton auroral events in relation to particle boundaries observed by NOAA 12, *J. Geophys. Res.*, *103*, 14,855–14,863, doi:10.1029/97JA02877.

Moen, J., H. C. Carlson, and P. E. Sandholt (1999), Continuous observation of cusp auroral dynamics in response to an IMF B_y polarity change, *Geophys. Res. Lett.*, *26*(9), 1243–1246, doi:10.1029/1999GL900224.

Moen, J., J. A. Holtet, A. Pedersen, B. Lybekk, K. Svenes, K. Oksavik, W. F. Denig, E. Lucek, F. Søraas, and M. André (2001), Cluster boundary layer measurements and optical observations at magnetically conjugate sites, *Ann. Geophys.*, *19*(10/12), 1655–1668, doi:10.5194/angeo-19-1655-2001.

Moen, J., M. Lockwood, K. Oksavik, H. C. Carlson, W. F. Denig, A. P. van Eyken, and I. W. McCrea (2004a), The dynamics and relationships of precipitation, temperature and convection boundaries in the dayside auroral ionosphere, *Ann. Geophys.*, *22*(6), 1973–1987, doi:10.5194/angeo-22-1973-2004.

Moen, J., K. Oksavik, and H. C. Carlson (2004b), On the relationship between ion upflow events and cusp auroral transients, *Geophys. Res. Lett.*, *31*, L11808, doi:10.1029/2004GL020129.

Moen, J., Y. Rinne, H. C. Carlson, K. Oksavik, R. Fujii, and H. Opgenoorth (2008), On the relationship between thin Birkeland current arcs and reversed flow channels in the winter cusp/cleft ionosphere, *J. Geophys. Res.*, *113*, A09220, doi:10.1029/2008JA013061.

Moen, J., H. Carlson, Y. Rinne, and Å. Skjæveland (2012), Multi-scale features of solar terrestrial coupling in the cusp ionosphere, *J. Atmos. Sol. Terr. Phy.*, *87–88*, 11–19, doi:10.1016/j.jastp.2011.07.002.

Newell, P. T., and C.-I. Meng (1988), The cusp and the cleft/boundary layer: Low-altitude identification and statistical local time variation, *J. Geophys. Res.*, *93*(A12), 14549–14556, doi:10.1029/JA093iA12p14549.

Newell, P. T., and C.-I. Meng (1989), On quantifying the distinctions between the cusp and the CLEFT/LLBL, in *Electromagnetic Coupling in the Polar Clefts and Caps*, vol. 278, edited by P. E. Sandholt and A. Egeland, pp. 87–101, NATO ASI Series, Springer, Netherlands, doi:10.1007/978-94-009-0979-3_6.

Newell, P. T., and C.-I. Meng (1992), Mapping the dayside ionosphere to the magnetosphere according to particle precipitation characteristics, *Geophys. Res. Lett.*, *19*(6), 609–612, doi:10.1029/92GL00404.

Newell, P. T., J. M. Ruohoniemi, and C.-I. Meng (2004), Maps of precipitation by source region, binned by IMF, with inertial convection streamlines, *J. Geophys. Res.*, *109*, A10206, doi:10.1029/2004JA010499.

Oksavik, K., F. Søraas, J. Moen, and W. J. Burke (2000), Optical and particle signatures of magnetospheric boundary layers near magnetic noon: Satellite and ground-based observations, *J. Geophys. Res.*, *105*(A12), 27,555–27,568, doi:10.1029/1999JA000237.

Oksavik, K., J. Moen, and H. C. Carlson (2004), High-resolution observations of the small-scale flow pattern associated with a poleward moving auroral form in the cusp, *Geophys. Res. Lett.*, *31*, L11807, doi:10.1029/2004GL019838.

Oksavik, K., J. Moen, H. C. Carlson, R. A. Greenwald, S. E. Milan, M. Lester, W. F. Denig, and R. J. Barnes (2005), Multi-instrument mapping of the small-scale flow dynamics related to a cusp auroral transient, *Ann. Geophys.*, *23*(7), 2657–2670, doi:10.5194/angeo-23-2657-2005.

Prölss, G. W. (2010), Density perturbations in the upper atmosphere caused by the dissipation of solar wind energy, *Surv. Geophys.*, *32*(2), 101–195, doi:10.1007/s10712-010-9104-0.

Rentz, S., and H. Lühr (2008), Climatology of the cusp-related thermospheric mass density anomaly, as derived from CHAMP observations, *Ann. Geophys.*, *26*(9), 2807–2823, doi:10.5194/angeo-26-2807-2008.

Rinne, Y., J. Moen, K. Oksavik, and H. C. Carlson (2007), Reversed flow events in the winter cusp ionosphere observed by the European Incoherent Scatter (EISCAT) Svalbard radar, *J. Geophys. Res.*, *112*, A10313, doi:10.1029/2007JA012366.

Rinne, Y., J. Moen, H. C. Carlson, and M. R. Hairston (2010), Stratification of east-west plasma flow channels observed in the ionospheric cusp in response to IMF B_y polarity changes, *Geophys. Res. Lett.*, *37*, L13102, doi:10.1029/2010GL043307.

Rishbeth, H., and O. K. Garriott (1969), *Introduction to Ionospheric Physics*, Acad. Press, Amsterdam.

Rother, M., K. Schlegel, and H. Lühr (2007), CHAMP observation of intense kilometer-scale field-aligned currents, evidence for an ionospheric Alfvén resonator, *Ann. Geophys.*, *25*(7), 1603–1615, doi:10.5194/angeo-25-1603-2007.

Ruohoniemi, J. M., R. A. Greenwald, K. B. Baker, J.-P. Villain, C. Hanuise, and J. Kelly (1989), Mapping high-latitude plasma convection with coherent HF radars, *J. Geophys. Res.*, *94*, 13,463–13,477.

Sadler, F. B., M. Lessard, E. Lund, A. Otto, and H. Lühr (2012), Auroral precipitation/ion upwelling as a driver of neutral density enhancement in the cusp, *J. Atmos. Sol. Terr. Phy.*, *87–88*, 82–90, doi:10.1016/j.jastp.2012.03.003.

Sandholt, P. E., B. Lybekk, A. Egeland, R. Nakamura, and T. Oguti (1989), Midday auroral breakup, *J. Geomagn. Geoelectr.*, *41*(4), 371–387, doi:10.5636/jgg.41.371.

Sandholt, P. E., C. J. Farrugia, J. Moen, Ø. Noraberg, B. Lybekk, T. Sten, and T. Hansen (1998), A classification of dayside auroral forms and activities as a function of interplanetary magnetic field orientation, *J. Geophys. Res.*, *103*(A10), 23,325–23,345, doi:10.1029/98JA02156.

Schlegel, K., H. Lühr, J.-P. St.-Maurice, G. Crowley, and C. Hackert (2005), Thermospheric density structures over the polar regions observed with CHAMP, *Ann. Geophys.*, *23*(5), 1659–1672, doi:10.5194/angeo-23-1659-2005.

Schunk, R. W., and A. F. Nagy (2009), *Ionospheres: Physics, Plasma Physics, and Chemistry*, 2 ed., Cambridge Atmospheric and Space Science Series, Cambridge Univ. Press, New York.

Shepherd, S. G. (2014), Altitude-adjusted corrected geomagnetic coordinates: Definition and functional approximations, *J. Geophys. Res. Space Physics*, *119*, 7501–7521, doi:10.1002/2014JA020264.

Skjæveland, Å., J. I. Moen, and H. C. Carlson (2011), On the relationship between flux transfer events, temperature enhancements and ion upflow events in the cusp ionosphere, *J. Geophys. Res.*, *116*, A10305, doi:10.1029/2011JA016480.

Smith, M. F., M. Lockwood, and S. W. H. Cowley (1992), The statistical cusp: A flux transfer event model, *Planet. Space Sci.*, *40*(9), 1251–1268, doi:10.1016/0032-0633(92)90082-Y.

St.-Maurice, J.-P., and W. B. Hanson (1982), Ion frictional heating at high latitudes and its possible use for an in situ determination of neutral thermospheric winds and temperatures, *J. Geophys. Res.*, *87*(A9), 7580–7602, doi:10.1029/JA087iA09p07580.

Strangeway, R. J. (2012), The equivalence of Joule dissipation and frictional heating in the collisional ionosphere, *J. Geophys. Res.*, *117*, A02310, doi:10.1029/2011JA017302.

Thayer, J. P., and J. Semeter (2004), The convergence of magnetospheric energy flux in the polar atmosphere, *J. Atmos. Sol. Terr. Phy.*, *66*(10), 807–824, doi:10.1016/j.jastp.2004.01.035.

Thébault, E. et al. (2015), International Geomagnetic Reference Field: The 12th generation, *Earth, Planets and Space*, *67*(1), 1–19, doi:10.1186/s40623-015-0228-9.

Valladares, C. E., J. Moen, P. E. Sandholt, W. F. Denig, and O. Troshichev (2002), Simultaneous observations of dayside aurora from Heiss Island and Ny Ålesund, *Geophys. Res. Lett.*, *29*(24), 2202, doi:10.1029/2002GL016001.

Walker, I. K., J. Moen, L. Kersley, and D. A. Lorentzen (1999), On the possible role of cusp/cleft precipitation in the formation of polar-cap patches, *Ann. Geophys.*, *17*(10), 1298–1305, doi:10.1007/s00585-999-1298-4.

Wannberg, G., et al. (1997), The EISCAT Svalbard radar: A case study in modern incoherent scatter radar system design, *Radio Sci.*, *32*(6), 2283–2307, doi:10.1029/97RS01803.

Watermann, J., P. Stauning, H. Lühr, P. T. Newell, F. Christiansen, and K. Schlegel (2009), Are small-scale field-aligned currents and magnetosheath-like particle precipitation signatures of the same low-altitude cusp?, *Adv. Space Res.*, *43*(1), 41–46, doi:10.1016/j.asr.2008.03.031.

Wilder, F. D., G. Crowley, S. Eriksson, P. T. Newell, and M. R. Hairston (2012), Ionospheric Joule heating, fast flow channels, and magnetic field line topology for IMF B_y-dominant conditions: Observations and comparisons with predicted reconnection jet speeds, *J. Geophys. Res.*, *117*, A11311, doi:10.1029/2012JA017914.

Yeoman, T. K., M. Lester, S. W. H. Cowley, S. E. Milan, J. Moen, and P. E. Sandholt (1997), Simultaneous observations of the cusp in optical, DMSP and HF radar data, *Geophys. Res. Lett.*, *24*(17), 2251–2254, doi:10.1029/97GL02072.

Zhang, B., W. Lotko, O. Brambles, M. Wiltberger, W. Wang, P. Schmitt, and J. Lyon (2012), Enhancement of thermospheric mass density by soft electron precipitation, *Geophys. Res. Lett.*, *39*, L20102, doi:10.1029/2012GL053519.